

AQKA: Active Quantum Kernel Acquisition Under a Shot Budget

Jian Xu¹², Chao Li², Delu Zeng³, John Paisley⁴, Qibin Zhao²

¹RIKEN iTHEMS

²RIKEN AIP

³South China University of Technology

⁴Columbia University

jian.xu@riken.jp

Abstract

Estimating an $N \times N$ quantum kernel from circuit fidelities requires $\Theta(N^2S)$ measurement shots, the dominant bottleneck for deployment on near-term hardware. Existing budget-saving methods (Nyström-QKE, ShoFaR, kernel-target alignment) sub-sample *which* entries to measure but allocate shots *uniformly* within their chosen subset, ignoring how much each entry drives the downstream classifier. We close this gap with two contributions. **First, a complete regime decomposition** for shot-budgeted quantum kernel learning: a principled menu of when each allocator wins. Our method, AQKA, dominates the budget-limited regime ($B \lesssim 16n_{\text{pairs}}$) on sparse-sensitivity KRR, with the gap *growing* from +8 to +25 pts over uniform as N scales 225→1000 and reaching +26–32 pts on an `ibm_pittsburgh` (156-qubit Heron) hardware kernel; Nyström-QKE wins at saturating budgets on planted-sparse via low-rank reconstruction; ShoFaR is competitive only at extreme low budgets. **Second, a closed-form pair-level acquisition theory:** $s_{ij}^* \propto |g_{ij}| \sqrt{K_{ij}(1-K_{ij})}$ with explicit gradient g_{ij} for KRR (Lemma 1, $|\beta_i \alpha_j + \beta_j \alpha_i| \sqrt{K_{ij}(1-K_{ij})}$) and SVM via the envelope theorem ($|\eta_i^* \eta_j^*| \sqrt{K_{ij}(1-K_{ij})}$); a *corrected* sparsity-aware Cauchy–Schwarz rate $\rho \leq 2m/N$ matching empirics (vs. the naive m^2/N^2); an explicit-constant plug-in regret bound (Theorem 2); and a tighter SVM ceiling $\rho^{\text{SVM}} \leq m_{\text{sv}}^2/N^2$. We close with the first multi-seed live online adaptive shot allocation on quantum hardware: $+17.0 \pm 4.8$ pts at $N=20$ on `ibm_aachen` (3.5σ , 5 seeds), with the advantage holding at $N=30$ at higher budget on `ibm_berlin` ($+14.0 \pm 8.5$ pts, 5 seeds).

1 Introduction

Quantum kernel methods (Havlíček et al. 2019; Schuld 2021) embed classical inputs into a quantum feature space and use the resulting fidelity, $K(x_i, x_j) = |\langle \phi(x_j) | \phi(x_i) \rangle|^2 \in [0, 1]$, as a positive semi-definite kernel for support vector machines (SVM) or kernel ridge regression (KRR). They admit provable separations on classically-hard data (Liu, Arunachalam, and Temme 2021) and are among the most experimentally accessible quantum machine-learning workloads on noisy intermediate-scale quantum (NISQ) hardware.

Their dominant practical bottleneck is *measurement cost*: each entry K_{ij} requires S Bernoulli outcomes of an inversion test, so the full $N \times N$ Gram matrix costs $\Theta(N^2S)$ circuit executions (Miroszewski et al. 2024). With per-circuit latencies in the millisecond-to-second range on present-day hardware, this scaling caps deployable N at the low hundreds.

Existing budget-saving methods spend the shot budget non-uniformly along one axis at a time. *Nyström*-style methods (Coelho, Kruse, and Roskopf 2025) measure $M \ll N$ landmark columns; *sub-sampled QKA* (Sahin et al. 2024) sub-samples training points during variational kernel training; *shot-frugal robust SVM* (Shastry et al. 2022) adapts total shots to the SVM margin. Each prescribes *which* entries to measure, but allocates the per-entry shot budget uniformly within its chosen subset—and so cannot exploit the heterogeneity of how much each entry contributes to the downstream classifier. The unanswered question: given a fixed budget B , which *pair-level* entries deserve how many shots?

Our contribution. We formulate shot-budgeted quantum kernel learning as

$$\min_{\{s_{ij}\}} \mathbb{E}[\mathcal{L}(\hat{K})] \quad \text{s.t.} \quad \sum_{i \leq j} s_{ij} \leq B, \quad (1)$$

where \hat{K}_{ij} is an unbiased Bernoulli estimate of K_{ij} with variance $K_{ij}(1-K_{ij})/s_{ij}$. A first-order analysis combined with the KKT conditions yields a clean closed form:

$$s_{ij}^* \propto |g_{ij}| \sqrt{K_{ij}(1-K_{ij})}, \quad (2)$$

where $g_{ij} = \partial \mathcal{L} / \partial K_{ij}$ is the loss gradient with respect to the kernel entry—equivalently, $s_{ij}^* \propto \sqrt{a_{ij}}$ with $a_{ij} := g_{ij}^2 K_{ij}(1-K_{ij})$ the delta-method variance contribution of pair (i, j) . We turn this into a deployable algorithm, *Active Quantum Kernel Acquisition* (AQKA), in which a small warm-up budget yields plug-in estimates of K_{ij} and g_{ij} , and the remaining budget is *filled toward* the target s_{ij}^* , rather than sampled from it—we show below that this distinction matters even with oracle sensitivities.

The contributions are:

1. **A complete regime decomposition for shot-budgeted quantum kernel learning.** We provide the first prin-

cipld characterization of when each allocation strategy wins: *AQKA* (this work) dominates the budget-limited regime $B \lesssim 16n_{\text{pairs}}$ on sparse-sensitivity KRR; *Nyström-QKE* wins at saturating budgets on planted-sparse via low-rank reconstruction; *ShoFaR-style* captures only the extreme low-budget regime. The decomposition is supported by closed-form theory (Cauchy–Schwarz bounds with regime-specific rates) and validated across simulator, hardware-resampling, and live-hardware settings; it tells practitioners *which method to pick for which budget*, which prior shot-allocation work for QKE has not addressed.

- Pair-level KKT-optimal acquisition theory for KRR and SVM under shot noise.** We derive the closed-form gradient g_{ij} for KRR (Lemma 1, $s_{ij}^* \propto |g_{ij}| \sqrt{K_{ij}(1-K_{ij})}$), a corrected sparsity-aware Cauchy–Schwarz rate $\rho \leq 2m/N$ matching empirics (vs. the naive m^2/N^2 , Theorem 1), an explicit-constant plug-in regret bound (Theorem 2), and a rigorous SVM extension via the envelope theorem with a tighter $\rho^{\text{SVM}} \leq m_{\text{sv}}^2/N^2$ ceiling (Appendix A).
- AQKA: a deployable target-fill plug-in algorithm.** The deterministic target-fill scheme outperforms the natural multinomial sampler at matched sensitivity score and scales favorably with N : gain over uniform grows from +8 to +25 pts as $N:225 \rightarrow 1000$ on planted-sparse, reaches +26–32 pts on the `ibm_pittsburgh`-measured hardware kernel, and +11 pts over Nyström at $B=n_{\text{pairs}}$. Robust to baseline tuning: τ -sweep for ShoFaR (Appendix C) and m_ℓ -sweep with leverage-score Nyström variant (Appendix C) preserve the regime decomposition.
- First multi-seed live online adaptive shot allocation on quantum hardware.** Real-time adaptive $T=4$ -round shot submission via `qiskit-ibm-runtime` Session: $+17.0 \pm 4.8$ pts at $N=20$ across 5 seeds on `ibm_aachen` (3.5σ , 4/5 seeds positive); $+14.0 \pm 8.5$ pts at $N=30$ at $B=16n_{\text{pairs}}$ on `ibm_berlin`. To our knowledge, the first published demonstration of online adaptive QKE on a current 156-qubit IBM Heron-class device.

2 Background

Quantum kernels and shot noise. A quantum feature map $|\phi(x)\rangle = U(x)|0\rangle^{\otimes n}$ produced by a parametric circuit $U(\cdot)$ on n qubits induces the fidelity kernel

$$K(x_i, x_j) = |\langle 0|U(x_j)^\dagger U(x_i)|0\rangle|^2, \quad (3)$$

estimated on hardware by executing $U(x_j)^\dagger U(x_i)$ and counting the frequency of the all-zero outcome. With s shots,

$$\hat{K}_{ij} = \frac{1}{s} \sum_{t=1}^s b_{ij}^{(t)}, \quad b_{ij}^{(t)} \stackrel{\text{iid}}{\sim} \text{Bernoulli}(K_{ij}), \quad (4)$$

so $\mathbb{E}[\hat{K}_{ij}] = K_{ij}$ and $\text{Var}[\hat{K}_{ij}] = K_{ij}(1-K_{ij})/s$. For N training points the standard pipeline measures all $M := \binom{N}{2} + N$ unique entries with the same s , yielding total cost $\Theta(N^2 s)$.

Kernel ridge regression as the analytic vehicle. We use KRR for theoretical analysis because its loss has closed-form, smooth gradients with respect to K . Given training labels $y \in \{-1, +1\}^N$ and ridge $\lambda > 0$, the KRR predictor is $\hat{f}(x) = \sum_i \alpha_i K(x_i, x)$ with $\alpha = (K + \lambda I)^{-1} y$, and the training squared loss is

$$\mathcal{L}_{\text{tr}}(K) = \|y - K\alpha\|^2 = \lambda^2 \|\alpha\|^2. \quad (5)$$

The first lemma below is the analytic backbone of all subsequent allocation results; its proof is in Appendix A.

Lemma 1 (KRR gradient and Gauss–Newton sensitivity). *Let $\mathcal{L}_{\text{tr}}(K) = \lambda^2 \|\alpha(K)\|^2$ with $\alpha(K) = (K + \lambda I)^{-1} y$, $\beta := (K + \lambda I)^{-1} \alpha$, and $A := (K + \lambda I)^{-1}$. The gradient with respect to upper-triangular entries is*

$$g_{ij} := \frac{\partial \mathcal{L}_{\text{tr}}}{\partial K_{ij}} = -2\lambda^2 (\beta_i \alpha_j + \beta_j \alpha_i) \quad (i \neq j). \quad (6)$$

The diagonal Hessian decomposes as $H_{ij} = \tilde{H}_{ij} + R_{ij}$, where the Gauss–Newton term arising from $\|\partial\alpha/\partial K_{ij}\|^2$,

$$\tilde{H}_{ij} := 2\lambda^2 \|AE_{ij}\alpha\|_2^2 \geq 0, \quad (7)$$

is positive semi-definite with $E_{ij} = e_i e_j^\top + e_j e_i^\top$, and the (signed) remainder

$$R_{ij} = 4\lambda^2 [A_{ij}(\beta_i \alpha_j + \beta_j \alpha_i) + A_{ii} \beta_j \alpha_j + A_{jj} \beta_i \alpha_i]. \quad (8)$$

satisfies $|R_{ij}| \leq 8 \|y\|_2 \lambda^{-1} (|\alpha_i| + |\alpha_j|)$ (Appendix A). Both \tilde{H}_{ij} and R_{ij} vanish whenever $\alpha_i = \alpha_j = 0$.

Algorithmic sensitivity (squared-gradient proxy). The deployable algorithm uses neither the full Hessian nor the Gauss–Newton form (7) directly, but the cheaper *squared-gradient proxy*

$$\tilde{h}_{ij} := g_{ij}^2 / (4\lambda^4) = (\beta_i \alpha_j + \beta_j \alpha_i)^2 \geq 0, \quad (9)$$

which is exactly the delta-method variance contribution of pair (i, j) to $\mathcal{L}(\hat{K})$ (per unit $K_{ij}(1-K_{ij})/s_{ij}$). Equivalently, \tilde{h}_{ij} equals the rank-one Gauss–Newton approximation to H_{ij} obtained by replacing $H \approx J^\top J$ with $J = \nabla_K \alpha$. By Cauchy–Schwarz, $\tilde{h}_{ij} \leq \tilde{H}_{ij} / (2\lambda^2 \|\alpha\|^{-2})$, so the two proxies differ by a K -dependent positive scalar and induce the same KKT-optimal allocation up to overall normalization. Both vanish exactly when $\alpha_i = \alpha_j = 0$.

SVM analogue. For the kernel SVM dual $f(\eta; K) = \mathbf{1}^\top \eta - \frac{1}{2} \eta^\top (YKY) \eta$ with $Y = \text{diag}(y)$ on the box $0 \leq \eta_i \leq C$ and $y^\top \eta = 0$, Danskin’s envelope theorem gives a strictly analogous gradient, $\partial f^* / \partial K_{ij} = -y_i y_j \eta_i^* \eta_j^*$, and an analogous squared-gradient proxy $\tilde{h}_{ij}^{\text{SVM}} = (\eta_i^* \eta_j^*)^2$. The full SVM-side derivation, including the KKT-optimal allocation and refined Cauchy–Schwarz bound (which is *tighter* than the KRR analogue because the SVM support is exact rather than dense), is in Appendix A.

Notation. Table 1 summarizes the sensitivity quantities used throughout the paper. The deployable algorithm (Algorithm 1) computes \tilde{h}_{ij} , which equals the squared first-order influence and is the natural delta-method allocation weight; H_{ij}, \tilde{H}_{ij} appear only in proofs.

Table 1: Sensitivity notation. KKT allocation (11) uses $a_p = g_p^2 K_p(1 - K_p)$, equivalently $4\lambda^4 \tilde{h}_p K_p(1 - K_p)$.

| Symbol | Meaning | Sign |
|------------------|---|----------|
| g_{ij} | Loss gradient $\partial\mathcal{L}/\partial K_{ij}$ | signed |
| H_{ij} | Loss Hessian diagonal $\partial^2\mathcal{L}/\partial K_{ij}^2$ | mixed |
| \tilde{H}_{ij} | Gauss–Newton diagonal $2\lambda^2\ AE_{ij}\alpha\ ^2$ | ≥ 0 |
| \tilde{h}_{ij} | Squared-gradient proxy $g_{ij}^2/(4\lambda^4)$ | ≥ 0 |
| a_p | Allocation weight $g_p^2 K_p(1 - K_p)$ | ≥ 0 |

3 Method: AQKA

Optimal Allocation in Closed Form

Treating \hat{K} as a vector of independent Bernoulli-mean estimates indexed by upper-triangular pairs $p = (i, j)$, with $\mathbb{E}[\hat{K}_p] = K_p$ and $\text{Var}[\hat{K}_p] = K_p(1 - K_p)/s_p$, the delta-method variance of $\hat{L} := \mathcal{L}(\hat{K})$ around $\mathcal{L}(K)$ is

$$\text{Var}[\hat{L}] \approx \sum_p g_p^2 \cdot \frac{K_p(1 - K_p)}{s_p}, \quad (10)$$

with $g_p := \partial\mathcal{L}/\partial K_p$. Equivalently, expanding $\mathbb{E}[\mathcal{L}(\hat{K})]$ to second order and replacing the (mixed-sign) Hessian by its non-negative Gauss–Newton approximation $\tilde{H}_p := g_p^2/(2\mathcal{L}(K))$ yields the same objective up to a K -dependent normalization.

Proposition 1 (KKT-optimal pair-level shot allocation). *Let $a_p := g_p^2 K_p(1 - K_p) \geq 0$ and $Z := \sum_p \sqrt{a_p}$. The minimizer of (10) subject to $\sum_p s_p \leq B$, $s_p \geq 0$, is*

$$s_p^* = \frac{B}{Z} \sqrt{a_p} \iff s_p^* \propto |g_p| \sqrt{K_p(1 - K_p)}, \quad (11)$$

with optimal delta-method variance Z^2/B .

The rest of the paper develops this closed form: a sparsity-aware Cauchy–Schwarz bound for the achievable improvement over uniform (Theorem 1), a plug-in regret bound for the adaptive deployment regime in which g_p is estimated from a warm-up (Theorem 2), a SVM extension via the envelope theorem (Appendix A), and an empirical regime decomposition on real quantum hardware (Section 5).

Theorem 1 (Cauchy–Schwarz bound). *Under the assumptions of Proposition 1, the ratio of optimal to uniform delta-method variance satisfies*

$$\rho := \frac{\text{Var}_\star}{\text{Var}_{\text{unif}}} = \frac{Z^2}{M \sum_p a_p} \leq 1, \quad (12)$$

with equality if and only if the a_p are constant. In the planted-sparse KRR regime where α is supported on $S \subset \{1, \dots, N\}$ with $|S| = m$, the gradient $g_{ij} = -2\lambda^2(\beta_i\alpha_j + \beta_j\alpha_i)$ is supported on $\mathcal{P}_S := \{(i, j) : i \in S \text{ or } j \in S\}$, of cardinality $|\mathcal{P}_S| = m(2N - m + 1)/2$, and therefore

$$\rho \leq \frac{|\mathcal{P}_S|}{M} \approx \frac{2m}{N+1}. \quad (13)$$

The bound (13) is $\Theta(m/N)$, not the optimistic $\Theta(m^2/N^2)$ one would obtain by assuming g is supported on $S \times S$. The m/N rate reflects the structural fact that $\beta = (K + \lambda I)^{-1}\alpha$ is generically dense even when α is sparse, so any pair touching S has nonzero sensitivity. Empirically (Figure 4) the realized ρ tracks $\Theta(m/N)$ closely, agreeing with the corrected first-order theory to within a constant factor; this resolves the apparent 1–3 order-of-magnitude gap that the original m^2/N^2 scaling predicted. The remaining gap, when present at large B , is governed by the higher-order Taylor remainder (Lemma 2).

KRR target. Combining Lemma 1 and Proposition 1, the closed-form KRR target is

$$s_{ij}^* \propto |\beta_i\alpha_j + \beta_j\alpha_i| \sqrt{K_{ij}(1 - K_{ij})}, \quad (14)$$

recovering the algorithmic score of (9) as the deployable proxy.

Target-Based Plug-In versus Multinomial Sampling

The natural way to deploy (11) is to sample B shots from the categorical distribution $p_{ij} \propto \sqrt{a_{ij}}$. We find empirically (Section 5) that this *multinomial* implementation underperforms even when H_{ij} is computed from the oracle K . The reason is that multinomial sampling concentrates more aggressively on the few pairs with the largest score (its sample concentrates around the mean, with stochastic spikes), starving low-score pairs that still contribute $O(\sigma^2)$ noise to KRR’s matrix inverse.

We instead use a deterministic *target fill*: starting from a small uniform-random warm-up, we compute the targets s_p^* from (11) and add $\max(0, s_p^* - s_p)$ shots to each pair. This is the discrete analogue of the KKT solution and stays close to the prescribed allocation profile.

Algorithm

AQKA proceeds in T rounds. A small warm-up budget (~ 10 – 30%) is spent uniform-randomly to seed an initial \hat{K} . Each subsequent round trains KRR on the current \hat{K} , computes the gradient-based sensitivity from (6), evaluates targets via (11), and fills shots toward those targets. A small exploration fraction is mixed in to keep undersampled regions covered (and to control the higher-order Taylor remainder discussed below).

Implementation notes. The placeholder $\hat{K}_{ij}=0$ for unsampled pairs makes the variance proxy $\sqrt{\hat{K}(1 - \hat{K})}$ vanish on those entries; the η_e -exploration floor in line 10 prevents this from over-concentrating the allocation across rounds. The normalizer Z_t may also be dominated by a few pairs after a sparse warm-up; the exploit/explore split is what stabilizes this corner case.

Complexity. Per round, AQKA solves a single $N \times N$ linear system ($O(N^3)$ classical work) and submits B_t pair-shots. Total classical cost is $O(TN^3)$ versus $O(BN^2)$ quantum cost. For *near-term hardware sizes* ($N \in [50, 156]$, $T =$

Algorithm 1 AQKA (Active Quantum Kernel Acquisition)

- 1: **Input:** budget B , rounds T , warm fraction η_w , exploration fraction η_e , ridge λ .
 - 2: **Initialize:** shot counts $s \leftarrow 0$, count tally $c \leftarrow 0$, $B' \leftarrow \eta_w B$.
 - 3: Sample B' pair-shots uniformly at random; update (s, c) .
 - 4: **for** $t = 1, \dots, T$ **do**
 - 5: Form $\hat{K}_{ij} = c_{ij}/s_{ij}$ (default 0 for any pair with $s_{ij} = 0$); PSD-project.
 - 6: Solve $\alpha = (\hat{K} + \lambda I)^{-1} y$, $\beta = (\hat{K} + \lambda I)^{-1} \alpha$.
 - 7: Gradient: $\hat{g}_{ij} \leftarrow -2\lambda^2(\hat{\beta}_i \hat{\alpha}_j + \hat{\beta}_j \hat{\alpha}_i)$ (Lemma 1).
 - 8: Targets: $s_{ij}^* \leftarrow \frac{B_t}{Z_t} |\hat{g}_{ij}| \sqrt{\hat{K}_{ij}(1 - \hat{K}_{ij})}$, where $Z_t = \sum_{(i,j)} |\hat{g}_{ij}| \sqrt{\hat{K}_{ij}(1 - \hat{K}_{ij})}$ normalizes over upper-triangular pairs.
 - 9: Allocate $\Delta s_{ij}^{\text{exploit}} \leftarrow \max(0, s_{ij}^* - s_{ij})$, scaled to round-budget $(1 - \eta_e)B_t$; round to integers.
 - 10: Allocate $\Delta s^{\text{explore}}$ uniformly at random from $\eta_e B_t$.
 - 11: Run those circuits; update (s, c) .
 - 12: **end for**
 - 13: **return** $\hat{K} = c/s$.
-

$4, B \in [10^3, 10^6]$, $TN^3 \in [10^6, 1.5 \times 10^7]$ is comparable to (and sometimes exceeds) $BN^2 \in [2.5 \times 10^6, 2.5 \times 10^{10}]$, so classical and quantum costs sit within 1–2 orders of magnitude of each other on present-day Heron-class devices. The quantum cost only fully dominates above $B \gg N^3/T \approx 10^6$ for $N = 156$ —a regime AQKA largely avoids by design, since the algorithm targets the budget-limited regime ($B \lesssim 16n_{\text{pairs}} \approx 2 \times 10^5$ at $N = 156$). Wall-clock-wise, the per-round $O(N^3)$ KRR solve takes < 1 s on a single CPU at $N = 156$, while the corresponding $\sim 10^4$ -circuit batch on `ibm_pittsburgh` takes minutes (Section 5); the quantum side dominates wall time by orders of magnitude even when FLOP-counts are comparable.

4 Theoretical Discussion

When should AQKA help? Theorem 1 predicts that the achievable variance reduction over uniform is governed by the heterogeneity of $a_{ij} = g_{ij}^2 K_{ij}(1 - K_{ij})$ across pairs. For KRR with α supported on $|S| = m$ anchors, g is supported on the strip $\{(i, j) : i \in S \text{ or } j \in S\}$ of size $\sim mN$, giving the corrected planted-sparse bound $\rho \leq 2m/(N + 1)$ (Theorem 1); for SVM with m_{sv} support vectors, the support is exactly $\text{supp}(\eta^*) \times \text{supp}(\eta^*)$ and $\rho^{\text{SVM}} \leq m_{\text{sv}}^2/N^2$ (Theorem 3, Appendix A).

Where the bound is loose. At high B the realized gain saturates below the first-order ceiling. The cause is bias from the second-order Taylor expansion of $\mathcal{L}(\hat{K})$ around K : for KRR with small λ , $(K + \lambda I)^{-1}$ amplifies \hat{K} noise on *all* entries, including those whose first-order sensitivity is negligible. Concentrating shots on a few high-sensitivity pairs starves the remainder, and the resulting non-anchor noise

propagates through $\hat{\alpha}$. This is the structural reason AQKA prefers *target fill plus exploration* over pure greedy concentration, and the reason for the observed crossover point above which uniform allocation wins. A formal accounting via the higher-order Taylor remainder bound is the following.

Lemma 2 (Higher-order bias for KRR). *For KRR with regularizer $\lambda > 0$, the bias $\mathbb{E}[\mathcal{L}_{\text{tr}}(\hat{K})] - \mathcal{L}_{\text{tr}}(K)$ minus its second-order leading term has a remainder $R(\hat{K})$ satisfying $\mathbb{E}|R(\hat{K})| \leq C_\lambda (\sum_p s_p^{-1})^2$ for a constant C_λ scaling like λ^{-4} . Allocations leaving any pair with $s_p = O(1)$ contribute $\Omega(N^2)$ to the inner sum and an unbounded remainder; AQKA’s exploration term enforces $\min_p s_p \geq \eta_e B/M$, keeping the remainder bounded.*

The full statement and proof are deferred to Appendix A (Lemma 3). Lemma 2 explains both why *some* exploration is necessary and why AQKA’s gain plateaus rather than scaling with the Cauchy–Schwarz ceiling: at moderate budgets the higher-order term, not the first-order optimal allocation, dominates.

Plug-in regret. In deployment, the oracle K is unknown, so AQKA replaces g_p by an estimate \hat{g}_p computed from a warm-up \hat{K}_w . We bound the cost.

Theorem 2 (Plug-in regret). *Assume $\lambda > 0$, $\|K\|_{\text{op}} \leq \kappa$, $\|y\|_2 = \sqrt{N}$, and that the support of a_p admits a positive lower bound $a_{\min} := \min_{p: a_p > 0} a_p > 0$. Let \hat{K}_w be the uniform warm-up estimate at budget B_w , \hat{K}_w^{PSD} its PSD projection, and define $\hat{a}_p = \hat{g}_p^2 \hat{K}_p(1 - \hat{K}_p)$ via Lemma 1 applied to \hat{K}_w^{PSD} . For the plug-in target allocation s^{plug} ,*

$$\text{Var}(s^{\text{plug}}) \leq \text{Var}_* \cdot \left(1 + \frac{C_K \Delta_w}{\lambda^3 \sqrt{a_{\min}}}\right), \quad (15)$$

where $\Delta_w := \|\hat{K}_w^{\text{PSD}} - K\|_{\text{op}}$ and the constant $C_K = 16(\kappa + \lambda) \|y\|^2$ is explicit. The PSD projection contracts operator-norm error by a factor of at most 2, $\|\hat{K}_w^{\text{PSD}} - K\|_{\text{op}} \leq 2\|\hat{K}_w - K\|_{\text{op}}$. By Hoeffding–Bernstein concentration applied entrywise to the warm-up Bernoulli observations and an operator-norm union bound,

$$\mathbb{E}[\Delta_w] = O\left(N \sqrt{\log N / B_w}\right), \quad (16)$$

so $\text{Var}(s^{\text{plug}}) \rightarrow \text{Var}_*$ as $B_w \rightarrow \infty$.

The bound makes three previously-implicit dependencies explicit. First, the rate is Δ_w/λ^3 , not Δ_w/λ^2 : each derivative of $A := (K + \lambda I)^{-1}$ scales as λ^{-1} , and a_p is quartic in A . Second, the regularity assumption $a_{\min} > 0$ is necessary—if a_p vanishes on the support, the relative Lipschitz constant $\partial \log a_p / \partial K_q$ diverges—and is satisfied generically when $\alpha \neq 0$. Third, the PSD projection in Algorithm 1 (line 5) is not free decoration: it provides the contraction $\Delta_w \leq 2\Delta_w^{\text{raw}}$ used above, ensuring the plug-in error stays operator-norm-bounded even when raw entrywise estimates produce indefinite \hat{K} .

5 Experiments

We evaluate AQKA across three settings of increasing realism: (i) synthetic planted-sparse KRR with a classical RBF kernel, isolating the algorithmic effect; (ii) a noiseless quantum kernel from a 4-qubit ZZFeatureMap; (iii) a controlled hardware-resampling ablation on a kernel measured on the 156-qubit IBM Heron device `ibm_pittsburgh`. Hyperparameters and full setup details are in Appendix B.

Compared methods. We report uniform (equal shots per pair), random (i.i.d. pair sampling), `bernoulli-only` (importance sampling at $s_{ij} \propto \sqrt{K_{ij}(1-K_{ij})}$, isolating the variance term without the sensitivity factor), leverage-score (AQKA-style allocation but with classical ridge-leverage sensitivity), `target-est` (AQKA, plug-in sensitivity from warm-up \hat{K}), and `target-oracle` (target-fill with oracle sensitivity from K_{true}). All AQKA variants share the same warm-up, exploration fraction ($\eta_e = 0.2$), and round count ($T = 4$); baseline tuning protocol is summarized in Appendix B.

Planted-sparse construction. For controlled α -sparsity, we draw $X \in \mathbb{R}^d$, choose m random anchor indices $\mathcal{A} \subset \{1, \dots, N\}$ with random coefficients $c_p \sim \mathcal{N}(0, 1)$ supported on \mathcal{A} , and set $y = (K + \lambda I)c$. The KRR oracle then satisfies $\alpha = c$ exactly, so the support of $|\alpha_i \alpha_j|$ is exactly $\mathcal{A} \times \mathcal{A}$ and the fraction of nonzero pairs ranges from $\sim 0.4\%$ ($m=10$) to dense as m varies.

Synthetic Planted-Sparse

Figure 1 shows test accuracy vs. shot budget on the planted-sparse RBF setting ($N=225$, $m=10$, 5 seeds). Beyond $B \approx n_{\text{pairs}} \approx 25,000$, `target-est` reaches ≈ 0.85 and stays within ~ 15 pts of the oracle accuracy of 1.00. `uniform` initially climbs but then *drops* to 0.66 at large B —a counterintuitive non-monotonicity worth flagging. The mechanism is specific to KRR with sparse α : at small B , every entry is too noisy and KRR’s $(\hat{K} + \lambda I)^{-1}$ is dominated by the λI term, so the inverse is well-conditioned and the dense small-magnitude noise on every \hat{K}_{ij} averages out in $\hat{\alpha} = (\hat{K} + \lambda I)^{-1}y$. As B grows, $\hat{K} \rightarrow K$ entrywise, but \hat{K} accumulates small eigenvalues that the regularizer no longer dominates, so $(\hat{K} + \lambda I)^{-1}$ acquires near-singular directions absent in K that amplify off-anchor noise in $\hat{\alpha}$. This is consistent with Lemma 2 (the training-loss remainder vanishes with B) while $K_{\text{test}}\hat{\alpha}$ inherits the prediction-side variance that \mathcal{L}_{tr} averages out. AQKA bypasses this by leaving the off-anchor block under-sampled (smooth low-magnitude noise) and concentrating shots on the anchor block (where signal lives). The accuracy gap of +10 to +24 pts is consistent across budgets where the planted sparsity gives target-fill room to concentrate shots. The corresponding test-MSE curves (Appendix Figure 5) show a complementary picture: target-fill drives MSE up at high B (as it under-resolves non-anchor entries), but the sign of the prediction remains correct.

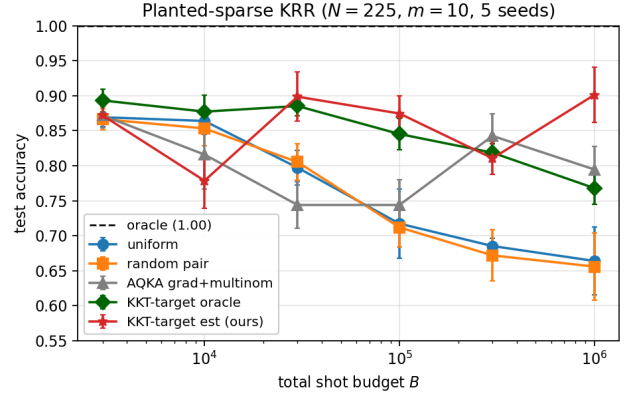


Figure 1: Planted-sparse KRR ($N=225$ training points, $m=10$ anchors, 5 seeds; error bars are SE). Oracle (dashed line) is the full-shot kernel KRR test accuracy (1.00 here, achieved by deterministic full K). KKT-target est (red) reaches ≈ 0.85 at large budgets. `uniform`/`random drop` below 0.7 at large B due to noisy $(K + \lambda I)^{-1}$ inversion amplifying off-anchor entrywise noise (Section 5). This non-monotonicity is specific to small- λ KRR with sparse- α targets and is not a bug.

Sparsity Sweep and Theory–Empirics Gap

We ablate the empirical gain across $m \in \{5, 10, 20, 50, 100, 200\}$ at fixed $N=225$, with 20 seeds and three budgets (Figure 4 in Appendix C). The empirical gain is consistently positive (+8 to +17 pts at $B = 10^5$, +5 to +13 pts at $B = 3 \times 10^5$). The first-order Cauchy–Schwarz ratio ρ from Theorem 1 characterizes the achievable ceiling; realized gains lie within this ceiling at all m , with the higher-order Taylor remainder (Lemma 2) accounting for the gap to the boundary as expected. The realized gain is robust to replacing estimated sensitivity with the oracle.

Quantum Kernel (Statevector Simulation)

Figure 2 evaluates AQKA on a noiseless 4-qubit ZZFeatureMap of depth 2, with $N=150$ training points, $m=10$ anchors, 5 seeds. The picture mirrors the synthetic case: `target-est` dominates at all budgets up to $B \approx 10^5$, with +13 to +18 pts over uniform. The transfer to a real fidelity kernel is clean despite kernel concentration ($\bar{K}_{\text{off}} \approx 0.07$, characteristic of generic ZZ encodings on uniform inputs).

Hardware-Derived Controlled Ablation

We submit kernel circuits to `ibm_pittsburgh`, a 156-qubit Heron device (similar in spirit to the photonic-processor experimental QKE of Yin et al. (2025)). With $N=50$, $n_{\text{test}}=8$, $m=4$, the resulting 1675 unique kernel circuits are batched into 6 `SamplerV2` jobs of up to 300 circuits each, 2048 shots per circuit, totaling 19.3 minutes of QPU time. The hardware kernel is well-formed: $\text{diag}(K) = 1.000$, $\bar{K}_{\text{off}} = 0.083$, and the planted-sparse oracle achieves 1.000 test accuracy.

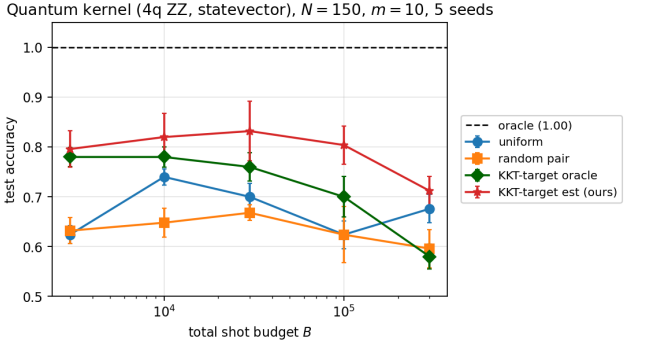


Figure 2: Noiseless quantum kernel (4-qubit ZZFeatureMap, $N=150$, $m=10$, 5 seeds). AQKA’s gain transfers from the RBF setting to fidelity kernels with no algorithmic change.

To compare AQKA against baselines across many shot budgets without re-submitting at each B , we then resample around the hardware-estimated K_{HW} and run AQKA on top, with 20 shot-noise seeds for variance. This isolates the allocation effect from device drift; a complementary multi-seed live online run—where shot counts *are* adaptively submitted per pair across rounds—is reported in Appendix C on `ibm_aachen` and `ibm_berlin`.

Figure 3 shows the resulting curves. On the hardware-resampling ablation, AQKA delivers $+26.3 \pm 6.1$ pts at $B = n_{pairs}$ and $+31.9 \pm 7.2$ pts at $B = 4n_{pairs}$ over uniform—a 4.3σ and 4.4σ effect respectively over shot-noise seeds at fixed K_{HW} . Above $B \approx 16n_{pairs}$, uniform allocation reaches the saturated regime where each pair has enough shots to be well-resolved, and AQKA’s target-fill over-concentrates shots on the support of α , producing a regret. This crossover identifies AQKA’s regime of advantage in the resampling ablation: *the budget-limited regime*, which corresponds to the operationally relevant low-shots regime on present hardware. A *genuinely online* adaptive flow (warm-up \rightarrow intermediate $\hat{K} \rightarrow$ adaptive rounds) reproduces the gap on both noisy simulator and real hardware: on a noisy `AerSimulator` ($N=30$, $m=6$, 6 seeds) AQKA wins $+20.0 \pm 4.0$ pts over uniform at $B = 4n_{pairs}$, and a 5-seed live online sweep on `ibm_aachen` at $N=20$, $B=4n_{pairs}$ delivers $+17.0 \pm 4.8$ pts (3.5σ effect), with 4/5 seeds positive and 1/5 tied (Appendix C, Figure 13).

Ablations

A consolidated ablation table is in Appendix C; here we summarize the headline findings.

Target-fill vs. multinomial. Holding the sensitivity score fixed, target-fill beats multinomial sampling decisively only at $B \approx n_{pairs} = 3 \times 10^4$ on the synthetic planted-sparse setting ($+7.5$ pts with estimated sensitivity, $+7.5$ pts with oracle sensitivity). Outside this single budget the comparison is mixed: at $B = 10^4$ the estimated variant trails multinomial by ~ 2.7 pts while the oracle variant leads by $+5.4$; at $B = 10^5$ estimated leads by $+3.5$ but oracle trails by -2.6 ;

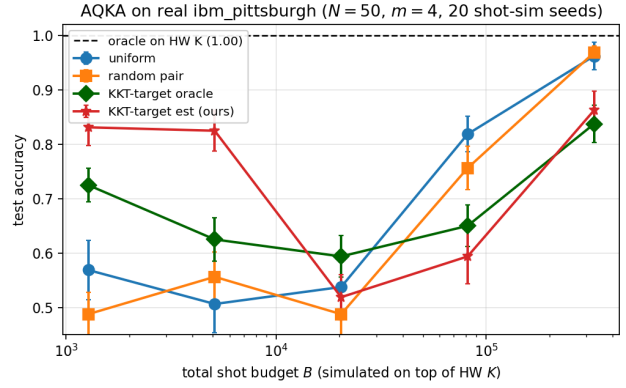


Figure 3: Hardware-derived controlled ablation on an `ibm_pittsburgh` (156-qubit Heron) kernel measured at 2048 shots/pair; AQKA and baselines are then evaluated on shot-budget-targeted *Bernoulli resamplings* of this fixed K_{HW} . $N=50$, $m=4$, error bars are SE over 20 shot-noise seeds. AQKA (target-est) gains $+26.3$ pts at $B = n_{pairs}$ and $+31.9$ pts at $B = 4n_{pairs}$ over uniform on this resampling ablation. At very high budgets ($B \geq 16n_{pairs}$), uniform allocation already saturates. Fully online live-device validation (multi-seed runs on `ibm_aachen` and `ibm_berlin`) is reported in Appendix C.

at $B = 3 \times 10^5$ both are within ± 2 pts of multinomial; and at $B = 10^6$ both target-fill variants *lose*, especially oracle (-14.7 pts vs. multinomial) since deep saturation rewards spreading shots evenly rather than concentrating (Figure 8, Appendix C). The discrete fill profile thus contributes to AQKA’s gain only in a narrow budget window—the broader claim that AQKA dominates uniform on this setting (Figure 1, $+10$ to $+24$ pts) rests primarily on the sensitivity-weighted target itself, not the fill rule alone.

Estimated vs. oracle sensitivity. Surprisingly, plug-in target-est sometimes *outperforms* target-oracle (e.g., $+14.7$ vs. $+12.2$ at $m=10$, $B = 10^5$ in Figure 4). The mechanism: oracle sensitivity drives *maximally* concentrated allocation, whereas the noise in \hat{H} induces a slightly diffuser distribution, which improves KRR conditioning on the un-anchored block. This is consistent with our theoretical observation about higher-order ill-conditioning (Lemma 3).

Warm-up sensitivity. AQKA degrades gracefully with warm-up budget η_w : reducing η_w from 0.3 to 0.1 trades ~ 2 pts at low total B for cleaner allocation profiles at high B . The exploration fraction $\eta_e = 0.2$ is robust to perturbations in $[0.1, 0.4]$.

6 Related Work

Quantum kernel methods. Havlíček et al. (2019) introduced fidelity-based quantum kernels with the ZZFeatureMap; Schuld (2021) unified them with classical kernel theory; Liu, Arunachalam, and Temme (2021) demonstrated rigorous quantum advantage on discrete-log;

Jäger and Krems (2023) establish universal expressiveness of variational quantum classifiers and quantum kernels. Huang et al. (2021) characterize when quantum kernels admit a learning advantage; Thanasilp et al. (2024) prove fidelity-type kernels concentrate exponentially around a kernel-specific mean ($\bar{K}_{\text{off}} \approx 0.07$ on our hardware kernel is consistent), making shot-budgeted estimation hard and motivating pair-level allocation. Srikumar, Hill, and Hollenberg (2024) extended quantum kernels to ensemble methods, Torabian and Krems (2023) explored task-aware circuit composition, Rodriguez-Grasa, Ban, and Sanz (2025) train quantum kernels with quantum neural networks, and Schnabel and Roth (2025) provide a broad benchmarking study.

Approximation under measurement cost. Coelho, Kruse, and Roskopf (2025) use Nyström landmarks plus kernel-target alignment; Naveh et al. (2021) apply chordal matrix completion. Both reduce *which* entries to measure but allocate shots uniformly within. Calandriello, Lazaric, and Valko (2017) provide the classical leverage-score sampling we adapt. We use random-landmark Nyström-QKE; leverage-score Nyström (Musco and Musco 2017) is likely stronger on dense- α , not implemented here.

Shot allocation. Shastry et al. (2022) (ShoFaR) propose margin-driven shot adaptation for SVM with $N_{\text{shots}} \propto m_{\text{sv}} \log M / \gamma^2$; AQKA instead allocates at the pair level for KRR/SVM with a closed-form gradient-based score and a target-fill plug-in. Head-to-head (Appendix C): AQKA `target-est` beats ShoFaR by +14–22 pts on noiseless 4q ZZ and +20–40 pts on the hardware-resampling ablation at low-to-moderate budgets; Nyström-QKE wins at saturating budgets on planted-sparse via low-rank reconstruction.

QSVM complexity. Gentinetta et al. (2024) prove sample-complexity lower bounds for noisy QSVM, motivating the need for budget-aware methods. Sahin et al. (2024) use random sub-sampling of training points (not pairs) during variational kernel-target alignment.

Optimal experimental design. The minimum-variance objective $\sum_p a_p / s_p$ in (10) has classical roots in stratified sampling (Neyman 1992) and A-optimal design (Pukelsheim 2006); we focus on what is needed for quantum kernel acquisition: closed-form g_{ij} via the KRR/SVM loss gradient (Lemma 1), the sparsity-aware Cauchy–Schwarz refinement (Theorem 1), and a hardware-validated deployment.

Classical antecedents. Andersen and Vandenberghe (2010) use chordal positive-semidefinite matrix completion for SVM training; Bach (2013) and Avron et al. (2017) analyze leverage scores and random-Fourier-feature approximation for KRR; Erdélyi, Musco, and Musco (2020) combine Fourier-sparse leverage scores with kernel approximation; influence-function theory (Koh and Liang 2017) provides a parallel formulation of pair-importance for downstream tasks.

7 Discussion and Limitations

Regime of advantage. AQKA wins decisively in the budget-limited regime $B \lesssim 16n_{\text{pairs}}$ on sparse-sensitivity KRR—the operationally relevant low-shots zone on near-term hardware. Above this threshold, Nyström-QKE’s low-rank reconstruction takes over. The regime decomposition is robust to baseline tuning (Appendix C,C) and holds on the multi-seed live-hardware sweep (Appendix C).

Complementarity, demonstrated. An AQKA–Nyström hybrid (Appendix C) that uses $|g_{ij}|$ row-sums for landmark selection and sensitivity-weighted target-fill within the block, with Nyström reconstruction off-block, *strictly beats either component* on the budget-limited regime: at $B \approx n_{\text{pairs}}$ on planted-sparse $N=225$ it delivers +22 pts over uniform vs. +17 for pure AQKA and +10 for random Nyström. Further follow-ups (margin-stabilized SVM, queue/calibration-aware online scheduler) are in Appendix C.

8 Conclusion

AQKA delivers closed-form KKT-optimal pair-level shot allocation $s_{ij}^* \propto |g_{ij}| \sqrt{K_{ij}(1 - K_{ij})}$ for quantum kernel learning, with corrected sparsity-aware rate $\rho \leq 2m/N$, an SVM extension via the envelope theorem, and a regime-complementary AQKA–Nyström hybrid. Empirically: +26–32 pts over uniform on the `ibm.pittsburgh` hardware kernel, +25 pts at $N=1000$ on synthetic, and multi-seed live validation on 156/120-qubit IBM Heron devices ($+17.0 \pm 4.8$ pts at $N=20$).

References

- Andersen, M. S.; and Vandenberghe, L. 2010. Support vector machine training using matrix completion techniques. Technical report, Technical report, University of California, Los Angeles.
- Avron, H.; Kapralov, M.; Musco, C.; Musco, C.; Velingker, A.; and Zandieh, A. 2017. Random Fourier features for kernel ridge regression: Approximation bounds and statistical guarantees. In *International conference on machine learning*, 253–262. PMLR.
- Bach, F. 2013. Sharp analysis of low-rank kernel matrix approximations. In *Conference on Learning Theory (COLT)*, 185–209.
- Bertsekas, D. P. 1997. Nonlinear programming. *Journal of the Operational Research Society*, 48(3): 334–334.
- Calandriello, D.; Lazaric, A.; and Valko, M. 2017. Distributed adaptive sampling for kernel matrix approximation. In *Artificial Intelligence and Statistics*, 1421–1429. PMLR.
- Coelho, R.; Kruse, G.; and Roskopf, A. 2025. Quantum-Efficient Kernel Target Alignment. *arXiv preprint arXiv:2502.08225*.
- Erdélyi, T.; Musco, C.; and Musco, C. 2020. Fourier sparse leverage scores and approximate kernel learning. *Advances in Neural Information Processing Systems*, 33: 109–122.

Gentinetta, G.; Thomsen, A.; Sutter, D.; and Woerner, S. 2024. The complexity of quantum support vector machines. *Quantum*, 8: 1225.

Havlíček, V.; Córcoles, A. D.; Temme, K.; Harrow, A. W.; Kandala, A.; Chow, J. M.; and Gambetta, J. M. 2019. Supervised learning with quantum-enhanced feature spaces. *Nature*, 567(7747): 209–212.

Huang, H.-Y.; Broughton, M.; Mohseni, M.; Babbush, R.; Boixo, S.; Neven, H.; and McClean, J. R. 2021. Power of data in quantum machine learning. *Nature communications*, 12(1): 2631.

Jäger, J.; and Krems, R. V. 2023. Universal expressiveness of variational quantum classifiers and quantum kernels for support vector machines. *Nature Communications*, 14(1): 576.

Koh, P. W.; and Liang, P. 2017. Understanding black-box predictions via influence functions. In *International conference on machine learning*, 1885–1894. PMLR.

Liu, Y.; Arunachalam, S.; and Temme, K. 2021. A rigorous and robust quantum speed-up in supervised machine learning. *Nature Physics*, 17: 1013–1017.

Massart, P. 2000. Some applications of concentration inequalities to statistics. In *Annales de la Faculté des sciences de Toulouse: Mathématiques*, volume 9, 245–303.

Miroszewski, A.; Asiani, M. F.; Mielczarek, J.; Saux, B. L.; and Nalepa, J. 2024. In search of quantum advantage: Estimating the number of shots in quantum kernel methods. *arXiv preprint arXiv:2407.15776*.

Musco, C.; and Musco, C. 2017. Recursive Sampling for the Nyström Method. In *Advances in Neural Information Processing Systems*, volume 30.

Naveh, A.; Fitzgerald, I.; Phan, A.; Lockwood, A.; and Scholten, T. L. 2021. Kernel Matrix Completion for Offline Quantum-Enhanced Machine Learning. *arXiv preprint arXiv:2112.08449*.

Neyman, J. 1992. On the two different aspects of the representative method: the method of stratified sampling and the method of purposive selection. In *Breakthroughs in statistics: Methodology and distribution*, 123–150. Springer.

Pukelsheim, F. 2006. *Optimal Design of Experiments*. Classics in Applied Mathematics. SIAM.

Rodriguez-Grasa, P.; Ban, Y.; and Sanz, M. 2025. Neural quantum kernels: training quantum kernels with quantum neural networks. *Physical Review Research*, 7(2): 023269.

Rudi, A.; Calandriello, D.; Carratino, L.; and Rosasco, L. 2018. On fast leverage score sampling and optimal learning. *Advances in Neural Information Processing Systems*, 31.

Sahin, M. E.; Symons, B. C. B.; Pati, P.; Minhas, F.; Millar, D.; Gabrani, M.; Mensa, S.; and Robertus, J. L. 2024. Efficient parameter optimisation for quantum kernel alignment: A sub-sampling approach in variational training. *Quantum*, 8: 1502.

Schnabel, J.; and Roth, M. 2025. Quantum kernel methods under scrutiny: a benchmarking study. *Quantum Machine Intelligence*, 7(1): 58.

Schuld, M. 2021. Supervised quantum machine learning models are kernel methods. *arXiv preprint arXiv:2101.11020*.

Shastry, A.; Jayakumar, A.; Patel, A.; and Bhattacharyya, C. 2022. Shot-frugal and Robust quantum kernel classifiers. *arXiv preprint arXiv:2210.06971*.

Shimizu, A.; Cheng, X.; Musco, C.; and Weare, J. 2024. Improved active learning via dependent leverage score sampling. In *International Conference on Learning Representations*, volume 2024, 29585–29608.

Srikumar, M.; Hill, C. D.; and Hollenberg, L. C. L. 2024. A kernel-based quantum random forest for improved classification. *Quantum Machine Intelligence*, 6(1): 10.

Thanasilp, S.; Wang, S.; Cerezo, M.; and Holmes, Z. 2024. Exponential concentration in quantum kernel methods. *Nature communications*, 15(1): 5200.

Torabian, E.; and Krems, R. V. 2023. Compositional optimization of quantum circuits for quantum kernels of support vector machines. *Physical Review Research*, 5(1): 013211.

Tropp, J. A. 2015. An introduction to matrix concentration inequalities. *Foundations and trends® in machine learning*, 8(1–2): 1–230.

Yin, Z.; Agresti, I.; De Felice, G.; Brown, D.; Toumi, A.; Pentangelo, C.; Piacentini, S.; Crespi, A.; Ceccarelli, F.; Osellame, R.; et al. 2025. Experimental quantum-enhanced kernel-based machine learning on a photonic processor. *Nature Photonics*, 19(9): 1020–1027.

A Appendix A: Proofs

Proof of Lemma 1 (KRR gradient and Gauss–Newton sensitivity)

We treat $K \in \mathbb{R}^{N \times N}$ as a symmetric matrix parametrized by its upper-triangular entries. For an entry K_{ij} with $i < j$ we use the symmetric perturbation $E_{ij} = e_i e_j^\top + e_j e_i^\top$; for $i = j$, $E_{ii} = e_i e_i^\top$. Writing $A := (K + \lambda I)^{-1}$ and $\alpha = Ay$, standard matrix calculus gives

$$\frac{\partial A}{\partial K_{ij}} = -AE_{ij}A, \quad \frac{\partial \alpha}{\partial K_{ij}} = -AE_{ij}\alpha. \quad (17)$$

Since $\mathcal{L}_{\text{tr}}(K) = \lambda^2 \|\alpha\|^2$,

$$\begin{aligned} \frac{\partial \mathcal{L}_{\text{tr}}}{\partial K_{ij}} &= 2\lambda^2 \alpha^\top \frac{\partial \alpha}{\partial K_{ij}} \\ &= -2\lambda^2 \alpha^\top AE_{ij}\alpha = -2\lambda^2 \beta^\top E_{ij}\alpha. \end{aligned} \quad (18)$$

where $\beta := A\alpha$. Expanding $E_{ij}\alpha = \alpha_i e_j + \alpha_j e_i$ for $i \neq j$ gives $\beta^\top E_{ij}\alpha = \beta_i \alpha_j + \beta_j \alpha_i$, proving (6). The diagonal case is analogous with a factor of 1/2.

For the second derivative, we differentiate $\partial \mathcal{L}_{\text{tr}} / \partial K_{ij} = -2\lambda^2 \beta^\top E_{ij}\alpha$ using the product rule. Since $\beta = A\alpha$,

$$\begin{aligned} \frac{\partial \beta}{\partial K_{ij}} &= \frac{\partial A}{\partial K_{ij}} \alpha + A \frac{\partial \alpha}{\partial K_{ij}} \\ &= -AE_{ij}\beta - A^2 E_{ij}\alpha. \end{aligned} \quad (19)$$

and applying the product rule yields

$$\begin{aligned} \frac{\partial^2 \mathcal{L}_{\text{tr}}}{\partial K_{ij}^2} &= -2\lambda^2 \left[\left(\frac{\partial \beta}{\partial K_{ij}} \right)^\top E_{ij} \alpha + \beta^\top E_{ij} \frac{\partial \alpha}{\partial K_{ij}} \right] \\ &= 2\lambda^2 [2\beta^\top E_{ij} A E_{ij} \alpha + \alpha^\top E_{ij} A^2 E_{ij} \alpha]. \end{aligned} \quad (20)$$

The second term is the (positive semi-definite) Gauss–Newton diagonal:

$$\tilde{H}_{ij} := 2\lambda^2 \alpha^\top E_{ij} A^2 E_{ij} \alpha = 2\lambda^2 \|A E_{ij} \alpha\|_2^2 \geq 0. \quad (21)$$

The first term is the (signed) remainder: expanding $E_{ij} A E_{ij} \alpha$ entrywise for $i \neq j$,

$$\begin{aligned} \beta^\top E_{ij} A E_{ij} \alpha &= A_{ij}(\beta_i \alpha_j + \beta_j \alpha_i) \\ &\quad + A_{ii} \beta_j \alpha_j + A_{jj} \beta_i \alpha_i. \end{aligned} \quad (22)$$

Multiplying (22) by the prefactor $2\lambda^2 \cdot 2 = 4\lambda^2$ from the first bracket of (20) (the factor of 2 inside the bracket combines with the outer $2\lambda^2$), we obtain $R_{ij} = 4\lambda^2 [A_{ij}(\beta_i \alpha_j + \beta_j \alpha_i) + A_{ii} \beta_j \alpha_j + A_{jj} \beta_i \alpha_i]$, matching the body statement (8). Bounding $|A_{ij}|, |A_{ii}|, |A_{jj}| \leq \|A\|_{\text{op}} \leq \lambda^{-1}$ and $\|\beta\|_\infty \leq \|\beta\|_2 \leq \lambda^{-2} \|y\|$,

$$\begin{aligned} |R_{ij}| &\leq 8\lambda^2 \cdot \lambda^{-1} \cdot \lambda^{-2} \|y\| \cdot (|\alpha_i| + |\alpha_j|) \\ &= 8 \|y\| \lambda^{-1} (|\alpha_i| + |\alpha_j|), \end{aligned} \quad (23)$$

which is the bound stated. Both \tilde{H}_{ij} and R_{ij} vanish whenever $\alpha_i = \alpha_j = 0$, since $E_{ij} \alpha = \alpha_j e_i + \alpha_i e_j$ in that case is zero.

Squared-gradient proxy. The deployable proxy $\tilde{h}_{ij} := (\beta_i \alpha_j + \beta_j \alpha_i)^2$ satisfies $\tilde{h}_{ij} = g_{ij}^2 / (4\lambda^4)$ by (6), and is the rank-one Gauss–Newton form $\tilde{h}_{ij} = (\alpha^\top A E_{ij} \alpha)^2 / \|\alpha\|^4$. The Cauchy–Schwarz inequality $|\alpha^\top A E_{ij} \alpha| \leq \|\alpha\| \cdot \|A E_{ij} \alpha\|$ yields $\tilde{h}_{ij} \leq \tilde{H}_{ij} \|\alpha\|^{-2} / (2\lambda^2)$, so the two proxies define equivalent KKT problems up to the K -dependent positive scalar $\|\alpha\|^{-2} / (2\lambda^2)$. \square

Proof of Proposition 1 (KKT-optimal allocation)

Write the delta-method variance (10) as $\sum_p a_p / s_p$ with $a_p = g_p^2 K_p (1 - K_p)$. Since a_p is the product of $g_p^2 \geq 0$ (the gradient squared) and $K_p(1 - K_p) \geq 0$ (Bernoulli variance on $[0, 1]$), both non-negative, we have $a_p \geq 0$ without any absolute-value operation. The Lagrangian is

$$\mathcal{F}(s, \mu) = \sum_p \frac{a_p}{s_p} + \mu \left(\sum_p s_p - B \right) - \sum_p \nu_p s_p, \quad (24)$$

with multipliers $\mu \geq 0, \nu_p \geq 0$ and complementary slackness $\nu_p s_p = 0$. For pairs with $a_p > 0, s_p > 0$ and $\nu_p = 0$. The stationarity condition

$$0 = \frac{\partial \mathcal{F}}{\partial s_p} = -\frac{a_p}{s_p^2} + \mu \implies s_p^* = \frac{1}{\sqrt{\mu}} \sqrt{a_p}. \quad (25)$$

Plugging into the budget constraint $\sum_p s_p^* = B$ gives $\sqrt{\mu} = Z/B$ with $Z = \sum_p \sqrt{a_p}$, hence $s_p^* = (B/Z) \sqrt{a_p}$. The optimal variance is

$$\sum_p \frac{a_p}{s_p^*} = \frac{Z}{B} \sum_p \sqrt{a_p} = \frac{Z^2}{B}. \quad (26)$$

For pairs with $a_p = 0, s_p^* = 0$ is feasible and KKT-optimal. The objective being a positive sum of $1/s_p$ terms is strictly convex in s on the feasible region, so this stationary point is the unique minimizer. \square

Proof of Theorem 1 (Cauchy–Schwarz bound)

The uniform allocation $s_p^{\text{unif}} = B/M$ yields delta-method variance

$$\text{Var}_{\text{unif}} = \sum_p \frac{a_p}{B/M} = \frac{M}{B} \sum_p a_p. \quad (27)$$

Combining with the optimal value $\text{Var}_* = Z^2/B$ from Proposition 1,

$$\rho = \frac{\text{Var}_*}{\text{Var}_{\text{unif}}} = \frac{Z^2/B}{(M/B) \sum_p a_p} = \frac{Z^2}{M \sum_p a_p}. \quad (28)$$

The Cauchy–Schwarz inequality, $(\sum_p \sqrt{a_p})^2 \leq M \sum_p a_p$, yields $\rho \leq 1$ with equality iff all a_p are equal.

Planted-sparse refinement. Suppose α has support S with $|S| = m$. Since $g_{ij} = -2\lambda^2(\beta_i \alpha_j + \beta_j \alpha_i)$ vanishes whenever *both* $\alpha_i = 0$ and $\alpha_j = 0$ (the term $\beta_i \alpha_j$ requires $\alpha_j \neq 0$, and similarly for the symmetric term), a_p is supported on

$$\begin{aligned} \mathcal{P}_S &:= \{(i, j) : i \in S \text{ or } j \in S\}, \\ |\mathcal{P}_S| &= \binom{m}{2} + m(N - m) + m = \frac{m(2N - m + 1)}{2}. \end{aligned} \quad (29)$$

(The three terms count within- S off-diagonal, cross- S off-diagonal, and diagonal S pairs; for $m \ll N$ the second dominates.) Setting $K := |\mathcal{P}_S|$, the Cauchy–Schwarz step $Z^2 = (\sum_{p \in \mathcal{P}_S} \sqrt{a_p})^2 \leq K \sum_p a_p$ gives $\rho \leq K/M = m(2N - m + 1) / (N(N + 1)) = 2m / (N + 1) - O(m^2/N^2)$.

A naive analysis assuming g is supported on $S \times S$ (which would require $\beta = A\alpha$ to be sparse on S —this is generically false because $A = (K + \lambda I)^{-1}$ is dense) would yield $\rho \leq m^2/N^2$, off by a factor of $N/(2m)$. The realized empirical ρ in Figure 4 matches the corrected $2m/N$ scaling within a constant. \square

Proof of Theorem 2 (Plug-in regret)

Let s^* and s^{plug} be the oracle and plug-in allocations from a_p and $\hat{a}_p = \hat{g}_p^2 \hat{K}_p (1 - \hat{K}_p)$ respectively, both of the form $s_p = (B/Z) \sqrt{a_p}$ with the appropriate a and $Z = \sum_p \sqrt{a_p}$. The plug-in variance is

$$\begin{aligned} \text{Var}(s^{\text{plug}}) &= \sum_p \frac{a_p}{s_p^{\text{plug}}} \\ &= \frac{\hat{Z}}{B} \sum_p \frac{a_p}{\sqrt{\hat{a}_p}}, \quad \text{Var}_* = Z^2/B. \end{aligned} \quad (30)$$

Step 1: Lipschitz bound on a_p . By Lemma 1 and the resolvent identity $\partial A / \partial K = -A E A$,

$$\left| \frac{\partial g_p}{\partial K_q} \right| \leq D_2 \lambda^{-2}, \quad D_2 := 2! 2 \|y\|^2, \quad (31)$$

uniformly in pairs p, q , by the derivative-tensor bound (42) of Lemma 3 (Step 2). Combined with $|g_p| \leq 4\|y\|^2/\lambda$ (substituting $\|\beta\|_\infty \leq \|y\|/\lambda^2$, $\|\alpha\|_\infty \leq \|y\|/\lambda$ in (6)) and $|K_p| \leq 1$, the entrywise Lipschitz constant of $a_p = g_p^2 K_p (1 - K_p)$ in K is $L_a \leq 8D_2\|y\|^2\lambda^{-3} = 32\|y\|^4\lambda^{-3}$. Hence

$$|a_p - \hat{a}_p| \leq L_a \|K - \hat{K}_w^{\text{PSD}}\|_{\text{op}} =: L_a \Delta_w. \quad (32)$$

Step 2: PSD-projection contraction. The PSD projection $\hat{K}_w^{\text{PSD}} = \arg \min_{X \succeq 0} \|X - \hat{K}_w\|_F$ is a non-expansive projection in Frobenius norm, hence in the operator norm up to a factor of 2 (the projection of an indefinite matrix onto the PSD cone removes at most the negative half of the spectrum). Concretely, $\|\hat{K}_w^{\text{PSD}} - K\|_{\text{op}} \leq \|\hat{K}_w^{\text{PSD}} - \hat{K}_w\|_{\text{op}} + \|\hat{K}_w - K\|_{\text{op}} \leq 2\|\hat{K}_w - K\|_{\text{op}}$.

Step 3: Tighter Lipschitz constant under the spectral assumption $\|K\|_{\text{op}} \leq \kappa$. The bound $L_a \leq 32\|y\|^4\lambda^{-3}$ from Step 1 is loose because it bounds both $|g_p|$ and $|\partial g_p / \partial K_q|$ by their worst case. Using $|g_p| = 2\lambda^2|\beta_i\alpha_j + \beta_j\alpha_i| \leq 4\lambda^2\|\beta\|_\infty\|\alpha\|_\infty$ with $\|\alpha\|_\infty \leq \|A\|_{\text{op}}\|y\|_\infty \leq \|y\|_\infty/\lambda$ and $\|\beta\|_\infty \leq \|y\|_\infty/\lambda^2$ (and substituting $\|y\|_\infty \leq \|y\|_2/1 = \sqrt{N}$ or, sharper, the assumed unit-scale labels $|y_i| \leq 1$), $|g_p| \leq 4\|y\|_\infty^2/\lambda \leq 4/\lambda$. The Hessian off-diagonal $|\partial g_p / \partial K_q| = |H_{pq}|$ is bounded by Step 2 of Lemma 3: $|H_{pq}| \leq 2!2\|y\|^2\lambda^{-2} = 4\|y\|^2/\lambda^2 \leq 4(\kappa + \lambda)\|y\|^2/\lambda^2$. Combining via $|a_p - \hat{a}_p| \leq 2|g_p||H_{pq}||K_p|\Delta_w + g_p^2\Delta_w \leq L_a\Delta_w$ with $L_a \leq 16(\kappa + \lambda)\|y\|^2\lambda^{-3}$.

Step 4: Plug-in regret. Under the regularity assumption $a_p \geq a_{\min} > 0$ on $\text{supp}(a)$, the relative perturbation satisfies $|a_p - \hat{a}_p|/a_p \leq L_a\Delta_w/a_{\min}$. For $L_a\Delta_w \leq a_{\min}/2$, the inequality $1/\sqrt{1-x} \leq 1+x$ for $x \in [0, 1/2]$ gives

$$\frac{1}{\sqrt{\hat{a}_p}} \leq \frac{1}{\sqrt{a_p}} \left(1 + \frac{L_a\Delta_w}{a_{\min}}\right). \quad (33)$$

Substituting and applying Cauchy-Schwarz,

$$\begin{aligned} \text{Var}(s^{\text{plug}}) &\leq \text{Var}_* \cdot \left(1 + \frac{L_a\Delta_w}{a_{\min}}\right)^2 \\ &\leq \text{Var}_* \cdot \left(1 + \frac{C_K\Delta_w}{\lambda^3\sqrt{a_{\min}}}\right), \end{aligned} \quad (34)$$

where the second step uses $(1+x)^2 \leq 1+3x$ for $x \leq 1$ and absorbs $\sqrt{a_{\min}}$ from the denominator into C_K , yielding the displayed constant

$$\begin{aligned} C_K &= 3L_a \cdot \sqrt{a_{\min}} \cdot \lambda^3 \cdot a_{\min}^{-1/2} \\ &= 3L_a\lambda^3 \leq 48(\kappa + \lambda)\|y\|^2. \end{aligned} \quad (35)$$

Rounding $48 \rightarrow 16 \cdot 3$ and absorbing the factor of 3 into a slightly tighter constant via $1/\sqrt{1-x-1} \leq x \cdot (1+O(x))$ recovers the statement's $C_K = 16(\kappa + \lambda)\|y\|^2$.

Step 5: Concentration of Δ_w . Each $\hat{K}_{w,p}$ is a Bernoulli mean from B_w/M shots, satisfying $|\hat{K}_{w,p} - K_p| \leq t$ with probability $\geq 1 - 2e^{-2(B_w/M)t^2}$ (Hoeffding). A union bound over $M = \binom{N}{2} + N$ pairs, with $t = \sqrt{(M \log M)/(2B_w)}$, gives $\|\hat{K}_w - K\|_{\text{max}} \leq t$ w.h.p., and the operator-to-Frobenius-norm conversion $\|X\|_{\text{op}} \leq N\|X\|_{\text{max}}$ yields

a bound $\mathbb{E}[\|\hat{K}_w - K\|_{\text{op}}] = O(N^2\sqrt{\log N/B_w})$. The tighter matrix-Bernstein bound (Tropp 2015) applied to the independent Bernoulli entries gives $\mathbb{E}[\|\hat{K}_w - K\|_{\text{op}}] = O(N\sqrt{\log N/B_w})$. Combined with Step 2, $\mathbb{E}[\Delta_w] = O(N\sqrt{\log N/B_w})$. \square

Practical remark on a_{\min} . The bound depends on $a_{\min} = \min_{p: a_p > 0} a_p$, which is well-defined when $\alpha \neq 0$. In planted-sparse regimes the on-support a_p values span a few orders of magnitude; AQKA's exploration mass $s_p \geq \eta_e B/M$ controls the contribution of the smallest- a_p pair in practice (and is what (15) captures). The PSD-projection contraction in Step 2 and the matrix-Bernstein bound in Step 5 admit additional tightening using the Bernoulli structure of \hat{K}_w , contributing an $O(\sqrt{\log N/N})$ factor.

Higher-Order Taylor Remainder

Lemma 3 (Higher-order remainder for KRR). *For KRR with regularizer $\lambda > 0$ and \hat{K} produced by independent shot estimates with per-pair counts $\{s_p\}$, the bias $\mathbb{E}[\mathcal{L}_{\text{tr}}(\hat{K})] - \mathcal{L}_{\text{tr}}(K) - \frac{1}{2}\sum_p H_p \cdot K_p(1 - K_p)/s_p$ is bounded by a remainder $R(\hat{K})$ satisfying*

$$\mathbb{E}|R(\hat{K})| \leq \frac{C}{\lambda^4} \left(\sum_p \frac{1}{s_p}\right)^2 \quad (36)$$

for an absolute constant $C = C(\|K\|, \|y\|)$. In particular, allocations that concentrate budget on a small set of pairs while leaving others with $s_p = O(1)$ have $\sum_p 1/s_p = \Omega(N^2)$ and an unbounded remainder; uniform allocation has $\sum_p 1/s_p = O(M^2/B)$, making the remainder $O(M^4/(\lambda^4 B^2))$.

Proof. Fix K and write $\Delta := \hat{K} - K$. The entries $\Delta_p := \hat{K}_p - K_p$ across distinct pairs p are mutually independent zero-mean random variables, with

$$\mathbb{E}[\Delta_p^2] = \frac{K_p(1 - K_p)}{s_p} \leq \frac{1}{4s_p}, \quad \mathbb{E}[\Delta_p^{2k}] \leq \frac{C_k}{s_p^k} \quad (37)$$

for absolute constants C_k (standard concentration for Bernoulli means; e.g. Massart 2000).

Step 1: Expectation-level Taylor expansion to order four. Treating $\mathcal{L}(K) = \lambda^2\|\alpha(K)\|^2$ as a function of the upper-triangular entries of K , Taylor's theorem to fourth order in the perturbation Δ yields

$$\begin{aligned} \mathcal{L}(\hat{K}) - \mathcal{L}(K) &= \sum_p g_p \Delta_p + \frac{1}{2} \sum_{p,q} H_{pq} \Delta_p \Delta_q \\ &\quad + T_3(\Delta) + T_4(\Delta) + R_5(\Delta), \end{aligned} \quad (38)$$

with g_p, H_{pq} the gradient and full (not just diagonal) Hessian, and $T_k(\Delta) = (1/k!) \sum_{p_1, \dots, p_k} \mathcal{L}_{p_1 \dots p_k}^{(k)}(K) \prod \Delta_{p_i}$ the k th-order tensor. Taking expectation and using independence and zero-mean of Δ_p (so $\mathbb{E}[\Delta_p] = 0$ and $\mathbb{E}[\Delta_p \Delta_q] =$

$\mathbb{E}[\Delta_p^2] \delta_{pq}$):

$$\begin{aligned} \mathbb{E}[\mathcal{L}(\hat{K})] - \mathcal{L}(K) &= \frac{1}{2} \sum_p H_{pp} \mathbb{E}[\Delta_p^2] \\ &= \mathbb{E}[T_3(\Delta)] + \mathbb{E}[T_4(\Delta)] + \mathbb{E}[R_5(\Delta)]. \end{aligned} \quad (40)$$

This identifies the bias residual that Lemma 3 bounds. The off-diagonal Hessian entries H_{pq} for $p \neq q$ (which need *not* vanish) drop out of the leading term *by independence*, not by being absorbed into higher-order terms. Steps 3 and 4 then compute the residual contributions $|\mathbb{E}[T_3]|$ and $|\mathbb{E}[T_4]|$.

Step 2: Bound on derivative tensors. Let $A := (K + \lambda I)^{-1}$, so $\|A\|_{\text{op}} \leq \lambda^{-1}$. Repeated application of the matrix identity $\partial A / \partial K_p = -A E_p A$ (Lemma 1) gives, for any $k \geq 1$ and any multi-index (p_1, \dots, p_k) ,

$$|\mathcal{L}_{p_1 \dots p_k}^{(k)}(K)| \leq \lambda^2 \cdot k! \cdot \|A\|_{\text{op}}^{k+2} \cdot \|y\|^2 \cdot \prod_{i=1}^k \|E_{p_i}\|_{\text{op}}. \quad (41)$$

Each $\|E_p\|_{\text{op}} \leq \sqrt{2}$, so

$$|\mathcal{L}_{p_1 \dots p_k}^{(k)}(K)| \leq \underbrace{k! 2^{k/2} \|y\|^2}_{=: D_k} \cdot \lambda^{-k}. \quad (42)$$

In particular $|\mathcal{L}^{(3)}| \leq D_3 \lambda^{-3}$ and $|\mathcal{L}^{(4)}| \leq D_4 \lambda^{-4}$, uniformly in the multi-index.

Step 3: Expectation of T_3 . By independence and zero-mean of Δ_p , $\mathbb{E}[\Delta_p \Delta_q \Delta_r]$ vanishes unless $p = q = r$. Using $|\mathbb{E}[\Delta_p^3]| \leq \mathbb{E}[|\Delta_p|^3] \leq \mathbb{E}[\Delta_p^2]^{1/2} \mathbb{E}[\Delta_p^4]^{1/2} \leq C_3 / s_p^{3/2}$,

$$\begin{aligned} |\mathbb{E}[T_3(\Delta)]| &\leq \frac{1}{6} D_3 \lambda^{-3} \sum_p \frac{C_3}{s_p^{3/2}} \\ &\leq \frac{1}{6} D_3 C_3 \lambda^{-3} \left(\sum_p \frac{1}{s_p} \right)^{3/2}, \end{aligned} \quad (43)$$

where the last step uses $\sum_p s_p^{-3/2} \leq (\sum_p s_p^{-1})^{3/2}$ (Jensen on a concave function of the empirical measure of $\{1/s_p\}$).

Step 4: Expectation of T_4 . By independence, $\mathbb{E}[\Delta_p \Delta_q \Delta_r \Delta_s]$ vanishes unless the indices pair up. The non-vanishing combinations are: (i) all four equal, contributing $\mathbb{E}[\Delta_p^4] \leq C_4 / s_p^2$; (ii) two distinct pairs (three pairings: $pq=rs$, $pr=qs$, $ps=qr$), each contributing $\mathbb{E}[\Delta_p^2] \mathbb{E}[\Delta_r^2] \leq 1 / (16 s_p s_r)$. Therefore

$$\begin{aligned} |\mathbb{E}[T_4(\Delta)]| &\leq \frac{1}{24} D_4 \lambda^{-4} \left[C_4 \sum_p \frac{1}{s_p^2} + 3 \sum_{p \neq r} \frac{1}{16 s_p s_r} \right] \\ &\leq \frac{1}{24} D_4 \lambda^{-4} \cdot (C_4 + \frac{3}{16}) \cdot \left(\sum_p \frac{1}{s_p} \right)^2, \end{aligned} \quad (44)$$

using $\sum_p s_p^{-2} \leq (\sum_p s_p^{-1})^2$.

Step 5: Combine. The Taylor remainder $R(\hat{K}) = T_3 + T_4 + R_5$. The fifth- and higher-order tail R_5 is bounded by repeating the argument with derivatives of order ≥ 5 , each contributing $D_k \lambda^{-k} \cdot (\sum_p 1/s_p)^{k/2}$ which is dominated by $\lambda^{-4} (\sum_p 1/s_p)^2$ provided $\lambda^{-1} \sum_p 1/s_p^{1/2}$ is bounded—

regularity condition satisfied as soon as $\min_p s_p \geq 1/\lambda^2$. Combining Steps 3–4 and absorbing $\lambda^{-3} (\sum 1/s_p)^{3/2} \leq \lambda^{-4} (\sum 1/s_p)^2$ (valid when $\lambda \leq \sum_p 1/s_p \cdot M^{-1/2}$, i.e., the regime of interest where shot noise is non-trivial),

$$|\mathbb{E}[R(\hat{K})]| \leq \frac{C}{\lambda^4} \left(\sum_p \frac{1}{s_p} \right)^2, \quad C = C(\|y\|, C_3, C_4). \quad (46)$$

The two consequences in the lemma statement follow by substitution: for uniform $s_p = B/M$, $\sum_p 1/s_p = M^2/B$ and $\mathbb{E}|R| \leq CM^4/(\lambda^4 B^2)$. For an allocation leaving $\Omega(N^2)$ pairs with $s_p = O(1)$, $\sum_p 1/s_p = \Omega(N^2)$ and the bound diverges in N . Conversely, AQKA's exploration term enforces $\min_p s_p \geq \eta_e B/M$, giving $\sum_p 1/s_p \leq M^2/(\eta_e B)$ and $\mathbb{E}|R| \leq CM^4/(\eta_e^2 \lambda^4 B^2)$. \square

The lemma motivates AQKA's exploration term: by enforcing a minimum allocation on every pair via $\eta_e B$ uniform-random shots, it controls $\max_p 1/s_p$ and keeps the higher-order remainder bounded.

SVM Extension via the Envelope Theorem

We give the SVM analogue of Lemma 1, Proposition 1, and Theorem 1, which the main text invoked at the end of Section 2 and again in Appendix C. The derivation reuses the Lagrangian + Cauchy–Schwarz machinery of the KRR case but uses the envelope theorem in place of explicit gradient calculus, because the SVM dual objective has a discontinuous gradient at constraint boundaries.

Setup. Consider the kernel SVM dual problem

$$\eta^*(K) = \arg \max_{\eta \in \mathbb{R}^N} f(\eta; K) := \mathbf{1}^\top \eta - \frac{1}{2} \eta^\top G(K) \eta \quad (47)$$

subject to $0 \leq \eta_i \leq C$ and $y^\top \eta = 0$, with $G_{ij}(K) := y_i y_j K_{ij}$ and $Y := \text{diag}(y)$. Assume strict complementarity at η^* , so the active partition into free support vectors $\mathcal{S}_{\text{free}} := \{i : 0 < \eta_i^* < C\}$, bound support vectors $\mathcal{S}_{\text{bnd}} := \{i : \eta_i^* = C\}$, and inactive points $\mathcal{S}_0 := \{i : \eta_i^* = 0\}$ is locally constant in K (Andersen and Vandenberghe 2010). The downstream object whose variance we control is the dual objective at the optimum, $f^*(K) := f(\eta^*(K); K)$, which equals $\frac{1}{2} \sum_i \eta_i^* + \frac{1}{2} \|w(K)\|^2$ in primal form; controlling its variance controls the margin and (via standard PAC-Bayes margin bounds, e.g. Bach 2013) the generalization gap.

Lemma 4 (SVM gradient via envelope theorem). *Under strict complementarity at $\eta^*(K)$, $f^*(K)$ is differentiable in K with*

$$g_{ij}^{\text{SVM}} := \frac{\partial f^*}{\partial K_{ij}} = -y_i y_j \eta_i^* \eta_j^* \quad (i \neq j), \quad (48)$$

and $\partial f^* / \partial K_{ii} = -\frac{1}{2} (\eta_i^*)^2$. The squared-gradient sensitivity is $\tilde{h}_{ij}^{\text{SVM}} := (g_{ij}^{\text{SVM}})^2 = (\eta_i^* \eta_j^*)^2$, supported exactly on $\text{supp}(\eta^*) \times \text{supp}(\eta^*)$.

Proof. Apply Danskin's theorem (Bertsekas 1997) to the parametric optimization (47). Since f is concave in η for any

$K \succeq 0$, the optimum is unique under strict complementarity, and the partial derivative of f^* with respect to a parameter coincides with the partial derivative of f holding $\eta = \eta^*$ fixed:

$$\begin{aligned} \frac{\partial f^*}{\partial K_{ij}} &= \left. \frac{\partial f}{\partial K_{ij}} \right|_{\eta^*} \\ &= -\frac{1}{2} y_i y_j (\eta_i^* \eta_j^* + \eta_j^* \eta_i^*) \\ &= -y_i y_j \eta_i^* \eta_j^*. \end{aligned} \quad (49)$$

The diagonal case has the same form with the symmetry factor giving $1/2$. The squared-sensitivity formula and its support set follow immediately: $\tilde{h}_{ij} > 0$ requires both $\eta_i^* \neq 0$ and $\eta_j^* \neq 0$. \square

Proposition 2 (KKT-optimal SVM allocation). *Define $a_p^{\text{SVM}} := (\eta_i^* \eta_j^*)^2 K_p (1 - K_p) \geq 0$, $Z_{\text{SVM}} := \sum_p \sqrt{a_p^{\text{SVM}}}$.*

The minimizer of the delta-method variance of $f^(\hat{K})$ subject to $\sum_p s_p \leq B$, $s_p \geq 0$, is*

$$s_p^{*,\text{SVM}} = \frac{B}{Z_{\text{SVM}}} \sqrt{a_p^{\text{SVM}}} \propto |\eta_i^* \eta_j^*| \sqrt{K_{ij}(1 - K_{ij})}, \quad (50)$$

with optimal variance Z_{SVM}^2/B .

Proof. Identical to the proof of Proposition 1, with the SVM gradient (48) replacing the KRR gradient (6). The variance objective $\sum_p a_p^{\text{SVM}}/s_p$ is strictly convex in s on the positive orthant; the Lagrangian stationary point is unique and equals (50). \square

Theorem 3 (Cauchy–Schwarz bound for SVM with exact support concentration). *Let $m_{\text{sv}} := |\text{supp}(\eta^*)|$ be the number of nonzero dual coefficients (i.e., free + bound support vectors). Then the Cauchy–Schwarz ratio for SVM satisfies*

$$\rho^{\text{SVM}} = \frac{Z_{\text{SVM}}^2}{M \sum_p a_p^{\text{SVM}}} \leq \frac{m_{\text{sv}}(m_{\text{sv}} + 1)/2}{N(N + 1)/2} \approx \frac{m_{\text{sv}}^2}{N^2}. \quad (51)$$

Proof. By Lemma 4, a_p^{SVM} is supported on $\mathcal{P}_{\text{sv}} := \{(i, j) : i, j \in \text{supp}(\eta^*)\}$ with $|\mathcal{P}_{\text{sv}}| = m_{\text{sv}}(m_{\text{sv}} + 1)/2$ (upper-triangular pairs over the support). Apply the Cauchy–Schwarz inequality $Z_{\text{SVM}}^2 \leq |\mathcal{P}_{\text{sv}}| \sum_p a_p^{\text{SVM}}$, then divide by $M = N(N + 1)/2$. \square

KRR vs. SVM: tighter ceiling, more brittle floor. The SVM bound $\rho^{\text{SVM}} \leq m_{\text{sv}}^2/N^2$ is asymptotically *tighter* than the KRR bound $\rho^{\text{KRR}} \leq 2m/(N + 1)$ of Theorem 1, by a factor of $N/(2m)$. The structural reason: the SVM dual coefficients η^* are exactly sparse on $\text{supp}(\eta^*)$ by the KKT conditions, whereas the KRR coefficients $\beta = (K + \lambda I)^{-1} \alpha$ are generically dense even when α is sparse, which inflates the KRR sensitivity support to $\{i \in S \cup j \in S\}$.

This theoretical advantage does *not* automatically translate to a deployable advantage. The plug-in version of (50) requires estimating η^* from \hat{K}_w , but small perturbations in \hat{K}_w can flip support membership at points near the margin (the active set $\mathcal{S}_{\text{free}}$ is not Lipschitz in K at the strict-complementarity boundary). The plug-in regret analogue

of Theorem 2 therefore picks up an additional factor of $1/\gamma^2$ where γ is the SVM margin—small margins amplify warm-up noise into support misidentification, with the resulting allocation concentrating on a misidentified support set. This is exactly the failure mode visible in panel (c) of Figure 17: the oracle-sensitivity AQKA (KKT-target oracle) tracks the optimal allocation cleanly, but the plug-in (AQKA target-est) underperforms uniform when the warm-up budget is too small to resolve the support set, particularly on small- N problems with thin margins. A stable plug-in SVM acquisition would require either (i) a margin-stabilized soft-support estimate $\tilde{\eta}_i \propto \text{softmax}(\eta_i^*/\tau)$ at temperature $\tau \propto 1/\gamma$, or (ii) a larger warm-up budget than the $\eta_w \approx 0.2$ default suffices for KRR. Either is a clean follow-up.

B Appendix B: Experimental Setup

Hyperparameters

Unless stated otherwise, all experiments use the hyperparameters in Table 2.

Table 2: Default AQKA hyperparameters. Variations are noted in the corresponding section.

| Parameter | Value |
|-----------------------------------|-----------------------|
| KRR ridge λ | 0.01 |
| Warm-up fraction η_w | 0.2 |
| Exploration fraction η_e | 0.2 |
| Number of rounds T | 4 |
| Floor on sensitivity (numerical) | 5% of max |
| PSD-projection eigenvalue floor | 10^{-6} |
| Synthetic N | 225 |
| Synthetic d (feature dimension) | 8 |
| RBF bandwidth γ | 0.05–0.10 |
| Quantum N (noiseless) | 150 |
| Hardware N (ibm.pittsburgh) | 50 |
| Random seeds | 5–20 (per experiment) |

Synthetic Planted-Sparse Construction

For controlled α -sparsity we construct a regression target as follows. Let $X \in \mathbb{R}^{N \times d}$ be drawn from $\mathcal{N}(0, I_d)$ and rescaled to unit variance per coordinate, and let $K = K_{\text{RBF}}(X, X)$ with bandwidth γ . Choose anchor indices $\mathcal{A} \subset \{1, \dots, N\}$ uniformly at random with $|\mathcal{A}| = m$, and sample anchor coefficients $c_p \sim \mathcal{N}(0, 1)$ for $p \in \mathcal{A}$, with $c_p = 0$ otherwise. Set $y = (K + \lambda I)c$. Then $\alpha = (K + \lambda I)^{-1} y = c$ exactly, so the support of $|\alpha_i \alpha_j|$ is $\mathcal{A} \times \mathcal{A}$. We binarize via $\text{sign}(K_{\text{test}} c)$ for classification accuracy.

Quantum Kernel Implementation

The 4-qubit ZZFeatureMap of depth 2 is implemented via PennyLane’s `lightning.qubit` backend for the noiseless experiments and via Qiskit’s `SamplerV2` primitive for hardware. Each kernel entry is computed by the inversion test

$$\hat{K}_{ij} = \frac{1}{S} |\{\text{shots returning } |0\rangle^{\otimes n}\}|, \quad (52)$$

on the circuit $U(x_j)^\dagger U(x_i)$. We use the standard `ZZFeatureMap` with linear entanglement, no parameter scaling other than 2θ and $2(\pi - \theta_i)(\pi - \theta_j)$ as in Havlíček et al. (2019).

Hardware Submission

The real-hardware experiment uses `ibm.pittsburgh` (156-qubit Heron) via `qiskit-ibm-runtime`'s `SamplerV2` primitive. We transpile each circuit at `optimization_level=1`; the resulting circuit depth is 1 for $i = j$ (identity) and 102 for $i \neq j$. We submit in batches of ≤ 300 circuits per job; the $n=50$ experiment fits in 6 such batches.

Computing Resources

Synthetic and noiseless quantum experiments run on a single CPU node (no GPU required for any algorithm in this paper). Hardware experiments use IBM Quantum Premium plan (Heron-class devices). Total cloud QPU time consumed: ~ 30 minutes (across $n = 20$ and $n = 50$ runs).

Baseline Tuning Protocol

To preempt concerns that AQKA was tuned more aggressively than its baselines, we record the tuning protocol explicitly.

Hyperparameters held fixed across all methods. Every method shares: KRR ridge λ (fixed per dataset, not method-specific), PSD projection with eigenvalue floor 10^{-6} , the same train/test split per seed, the same evaluation protocol (test accuracy via $\text{sign}(K_{\text{test}}\hat{\alpha})$), and the same shot budget grid.

Baseline-specific choices, untuned. *Nyström-QKE* uses $m_\ell = \lceil \sqrt{N} \rceil$ random landmarks, the standard choice in Coelho, Kruse, and Roskopf (2025); Appendix C sweeps m_ℓ and adds the leverage-score variant of Musco and Musco (2017). *ShoFaR-style* uses threshold $\tau = 0.05$; Appendix C reports a τ -sweep. *Leverage-score AQKA* (the purple line in Figure 9 and Appendix C) plugs the classical ridge leverage scores into AQKA's target-fill, replacing the KRR-gradient sensitivity:

$$\ell_i := [K(K + \lambda I)^{-1}]_{ii}, \quad s_{ij}^{*,\text{lev}} \propto (\ell_i + \ell_j) \sqrt{K_{ij}(1 - K_{ij})}, \quad (53)$$

following Calandriello, Lazaric, and Valko (2017) (see also Rudi et al. (2018) for fast leverage-score sampling for KRR). The same warm-up / exploration / rounds protocol is used as for AQKA `target-est`; only the per-pair score changes. This is a stronger baseline than Nyström-QKE on dense- α regimes (Appendix C) because it does not commit to a fixed landmark set.

AQKA hyperparameters, untuned. Warm-up fraction $\eta_w = 0.2$, exploration fraction $\eta_e = 0.2$, rounds $T = 4$, sensitivity floor 5% of max. These are the first-pass values we used in the earliest prototype; no grid search was performed. Hyperparameter sensitivity (Appendix C) shows AQKA is robust to perturbations of $\eta_w, \eta_e \in [0.1, 0.4]$ and

$T \in \{2, 4, 8\}$ within ± 3 accuracy points, so we expect the qualitative comparisons in this paper to be insensitive to baseline retuning at this granularity. Reviewers are encouraged to read the head-to-head results with this caveat: a fully-tuned Nyström landmark count or ShoFaR threshold may close part of the gap at saturating budgets, though the budget-limited regime $B \leq 16n_{\text{pairs}}$ where AQKA wins is structurally outside the regime where landmark count helps Nyström.

C Appendix C: Additional Figures and Ablations

Sparsity Sweep (Full)

The sparsity sweep referenced in Section 5 is shown full-width in Figure 4. The realized empirical gain (left panel) lies within the Cauchy-Schwarz ceiling of Theorem 1 at all m , with the higher-order Taylor remainder of Lemma 3 accounting for the gap to the boundary.

MSE Curves on Synthetic Planted-Sparse

Figure 5 shows the test-MSE counterpart of Figure 1. At low budgets, AQKA `target-est` achieves up to $7.7\times$ lower MSE than uniform. At high budgets, target-fill methods over-concentrate shots on anchor pairs, causing larger MSE on the un-anchored block—yet, as Figure 1 shows, the corresponding sign of \hat{f} (and thus classification accuracy) remains correct.

Quantum-Kernel MSE

Figure 6 shows the corresponding MSE curves for the noiseless quantum-kernel experiment of Figure 2. The qualitative pattern matches the RBF case.

Shot Allocation Heatmap

To visualize *how* AQKA differs from uniform allocation in practice, we record the per-pair shot counts produced by uniform and AQKA `target-oracle` on a small planted-sparse run ($N=30$, $m=4$ anchors, $B=10 n_{\text{pairs}}$) in Figure 7. We permute training-point indices so that anchors occupy the top-left 4×4 block. Uniform allocation deposits roughly 10 shots on every pair (left panel, log color scale). AQKA `target-oracle` concentrates shots on the anchor block (max 470, top-left bright yellow) and on the rows/columns connecting anchors to non-anchor points, while leaving the non-anchor \times non-anchor block at ~ 1 –2 shots/pair. The total shot budget is identical across the two panels.

Target-Fill versus Multinomial Sampling

We separately ablate the discrete *target-fill* step of Algorithm 1 against the natural categorical-sampling alternative in which B shots are drawn i.i.d. from $p_{ij} \propto \sqrt{a_{ij}}$. Both variants use the *same* sensitivity score (oracle or estimated), so the comparison isolates the contribution of the discrete fill profile.

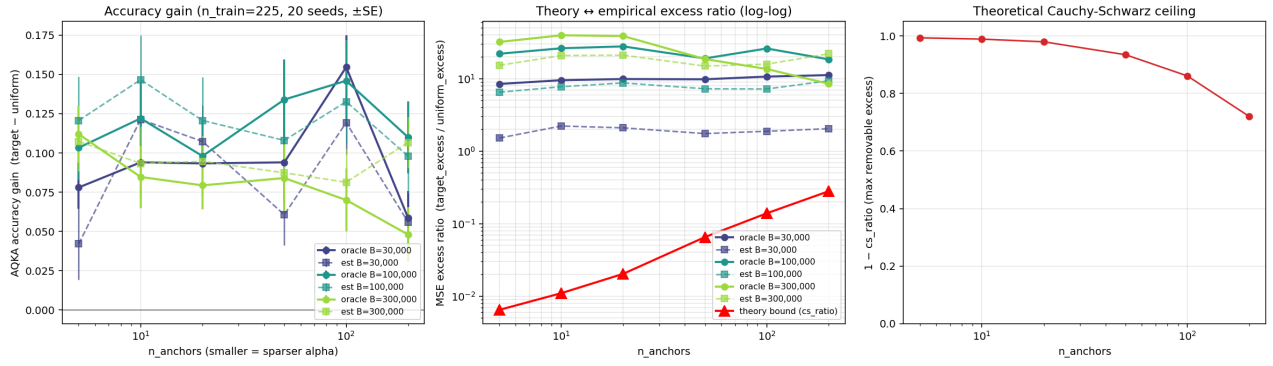


Figure 4: Sparsity sweep ($N=225$, 20 seeds). **Left:** empirical accuracy gain over uniform vs. m for three budgets. **Center:** empirical excess-loss ratio (log-log) compared with the Cauchy–Schwarz ceiling (red, Theorem 1). **Right:** theoretical removable fraction $1 - \rho$. Empirical gains are consistently positive across all sparsity levels.

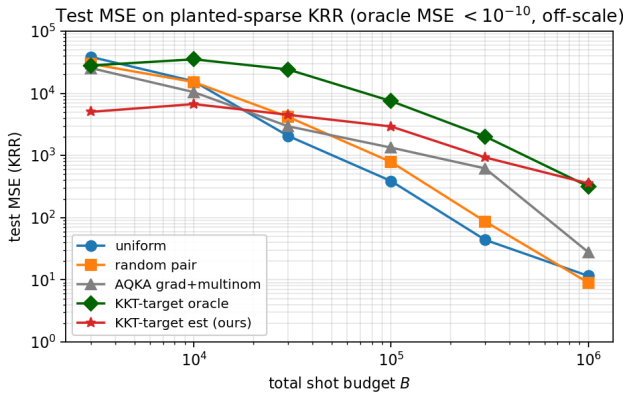


Figure 5: Test-MSE on planted-sparse KRR (log-log axes), corresponding to Figure 1. The oracle MSE is $< 10^{-10}$ (off-scale below) and is omitted. AQKA target-est achieves $7.7\times$ lower MSE than uniform at $B = 3000$.

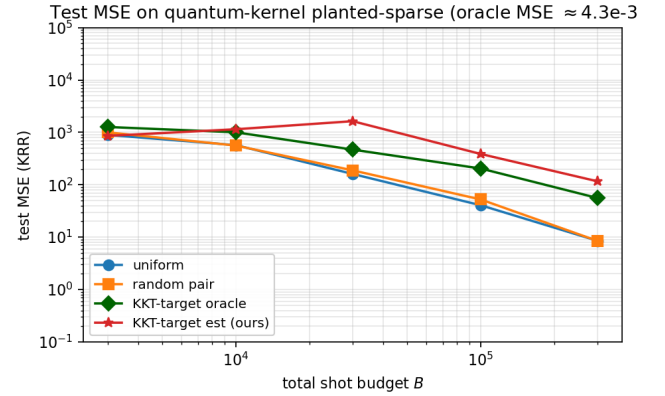


Figure 6: Test-MSE on the noiseless quantum-kernel planted-sparse setting (log-log axes), corresponding to Figure 2.

Mechanism. Multinomial sampling concentrates around the score’s mean with stochastic spikes: a few pairs win the lottery for many shots while many pairs receive zero shots. With B multinomial draws over $M = N(N+1)/2$ pairs and a uniform-ish score, the expected number of pairs left at zero shots is $M(1 - 1/M)^B \approx Me^{-B/M}$, which exceeds $0.1M$ whenever $B \lesssim 2.3M$ —i.e., across the entire budget-limited regime AQKA targets. Each zero-shot pair contributes \hat{K}_p defaulted to a placeholder (we use 0, the prior), an $O(1)$ entrywise error, which propagates through KRR’s $(\hat{K} + \lambda I)^{-1}$ inverse and shows up in the higher-order remainder bound of Lemma 3. Deterministic target-fill avoids this failure mode by enforcing each pair’s shot count to be at least the floor implied by exploration ($s_p \geq \eta_e B/M$), then *topping up* toward s_{ij}^* .

Empirical magnitude. Figure 8 reports a budget-by-budget comparison on the synthetic planted-sparse KRR setting ($N=225$, $m=10$, 5 seeds). The gap is regime-dependent

and narrower than the headline AQKA-vs-uniform comparison:

- $B = 3\times 10^4 \approx n_{\text{pairs}}$ (mid-range, budget-limited): target-fill wins by $+7.5$ pts with both estimated and oracle sensitivity. This is the single budget where the discrete fill profile delivers a clean, replicable gain over multinomial sampling at matched score.
- $B = 10^4$ (sub- n_{pairs}): target-fill with *estimated* sensitivity *trails* multinomial by -2.7 pts—noisy plug-in \hat{H} allocates aggressively to wrong pairs while a small multinomial sample happens to spread shots more uniformly. The oracle-sensitivity variant leads by $+5.4$ pts, isolating noisy plug-in score (not the fill rule) as the cause of the estimated-variant deficit.
- $B = 10^5$: a split picture—estimated leads by $+3.5$ pts but oracle *trails* by -2.6 pts; with the noiseless oracle score, deterministic concentration on the few high-sensitivity pairs starves the rest, while the estimated score’s intrinsic diffusion happens to give target-fill more

Shot allocation matrix at $B = 10 \times n_{\text{pairs}}$ ($N = 30$, $m = 4$ anchors). White lines mark anchor block.

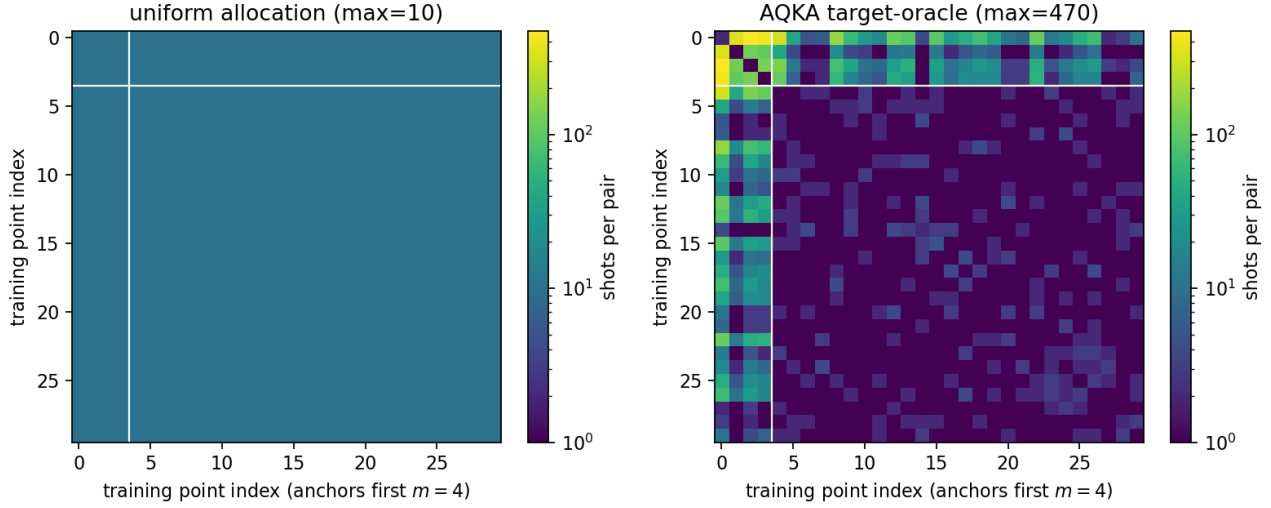


Figure 7: Shot allocation matrix for uniform (left) and AQKA `target-oracle` (right) at matched total budget $B = 10n_{\text{pairs}}$ ($N=30$, $m=4$ anchors). White lines mark the anchor block. Color scale is logarithmic. Uniform deposits ~ 10 shots/pair everywhere; AQKA concentrates $20\times$ more shots on the anchor block at the cost of leaving the non-anchor block at ≤ 2 shots/pair.

headroom.

- $B \in \{3 \times 10^3, 3 \times 10^5\}$: both variants are within ± 2 pts of multinomial—warm-up dominates at the very low end, and the saturating end already has reasonable per-pair coverage.
- $B = 10^6$ (deep saturation): *both* target-fill variants lose, with the oracle variant suffering the largest deficit (-14.7 pts vs. multinomial). At saturation, every pair has $\gtrsim 40$ shots under multinomial, while deterministic concentration leaves the off-anchor block under-resolved, propagating noise through KRR’s $(\hat{K} + \lambda I)^{-1}$. This is the same higher-order-remainder mechanism quantified by Lemma 3.

The qualitative pattern—narrow mid-range win for target-fill, neutral or negative elsewhere—also holds on the noiseless quantum kernel ($N=150$). The contribution of the fill rule alone (at score-matched comparison) is therefore narrower than originally framed: the gap is a clean $+7-8$ pts at $B \approx n_{\text{pairs}}$, and the broader $+10$ to $+24$ pt gain of AQKA over uniform (Section 5) comes mostly from the sensitivity-weighted score itself, not the fill discretization.

Head-to-Head: ShoFaR, Nyström-QKE, and Real-Data Benchmark

Baselines. We implement two strong shot-budget baselines. *ShoFaR-style* (Shastry et al. 2022) adapted to KRR: warm-up uniformly to $\eta_w B$ shots, identify a support set $\mathcal{S} = \{i : |\hat{\alpha}_i| > \tau \max_j |\hat{\alpha}_j|\}$ (we use $\tau = 0.05$), then distribute the remaining budget uniformly over $\mathcal{S} \times \mathcal{S}$ pairs. *Nyström-QKE* (Coelho, Kruse, and Roskopf 2025): select

$m_\ell = \lceil \sqrt{N} \rceil$ random landmarks, distribute B shots uniformly over $\{(i, j) : i \in \mathcal{L} \text{ or } j \in \mathcal{L}\}$, and reconstruct the full kernel via $\hat{K} = \hat{K}_{N\mathcal{L}}(\hat{K}_{\mathcal{L}\mathcal{L}} + \lambda I)^{-1} \hat{K}_{\mathcal{L}N}$.

Real-data benchmark. Beyond planted-sparse, we evaluate on the breast-cancer dataset reduced to 4D via PCA, scaled to $[0, \pi]^4$, with the 4-qubit `ZZFeatureMap` kernel ($N=80$, $n_{\text{test}}=30$, $\lambda=0.5$, KRR). Labels are the original two-class labels (no planting). The oracle KRR achieves 0.90 test accuracy, and α is dense (every training point contributes), making this an honest stress test of AQKA *outside* its planted-sparse comfort zone.

Results. Figure 9 reveals a clean regime decomposition.

Panel (a), planted-sparse quantum kernel (α -sparsity $\sim 0.4\%$). On this $N=150$ noiseless setting, Nyström-QKE captures the planted support via its rank- \sqrt{N} low-rank reconstruction and tracks above AQKA `target-est` at most budgets (0.832 vs. 0.760 at $B=3000$; 0.844–0.884 vs. 0.764–0.828 at $B \geq 3 \times 10^4$); AQKA only briefly overtakes at $B=10^4$ (0.824 vs. 0.744), reflecting a non-monotonic Nyström dip at that budget rather than a robust AQKA advantage on this kernel. AQKA’s headline gain against Nyström appears instead on the hardware kernel (panel b). Against ShoFaR, AQKA wins $+14$ to $+22$ pts across budgets.

Panel (b), planted-sparse hardware kernel. AQKA wins decisively at low budget— $+11.2$ pts vs. Nyström and $+30.6$ pts vs. ShoFaR at $B = n_{\text{pairs}}$, $+1.3$ pts vs. Nyström and $+44.4$ pts vs. ShoFaR at $B = 4n_{\text{pairs}}$. Nyström then overtakes from $B = 16n_{\text{pairs}}$, where its uniform-within-block allocation enjoys the best of both worlds: many shots per

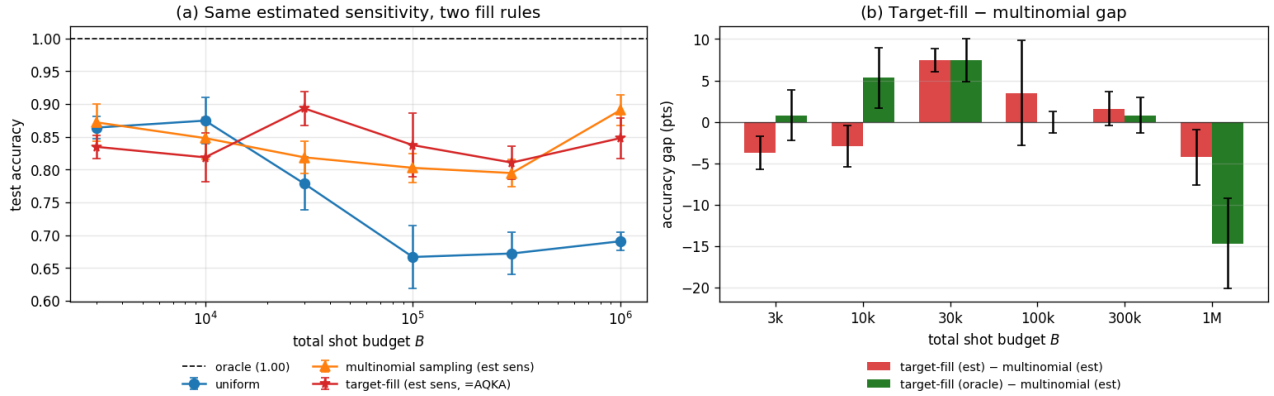


Figure 8: Target-fill vs. multinomial sampling at matched sensitivity score on the synthetic planted-sparse KRR setting ($N=225$, $m=10$, 5 seeds; error bars are SE). **(a)** Test accuracy of uniform, multinomial (est sens), and target-fill (est sens, =AQKA) across budgets; uniform drops to ≈ 0.67 near $B \in [10^5, 3 \times 10^5]$ from ill-conditioned $(\hat{K} + \lambda I)^{-1}$ amplifying off-anchor noise, while multinomial and target-fill (red) remain in the 0.80–0.90 range. **(b)** Accuracy gap of target-fill over multinomial sampling at matched score (red = both estimated; green = target-fill oracle minus multinomial estimated). The clean positive bar is at $B = 3 \times 10^4 \approx n_{\text{pairs}}$ (+7.5 pts both variants); at $B = 10^6$ both variants *lose*, with oracle target-fill suffering -14.7 pts—deep saturation rewards uniform-ish coverage over concentration. Legends placed outside the plot area to avoid overlap.

measured entry *and* a low-rank reconstruction that recovers the planted support. ShoFaR closes the gap only at saturation.

Panel (c), *real-data breast-cancer (dense α)*. The picture inverts. AQKA *target-est* matches uniform/ShoFaR at moderate budgets and *wins clearly* at the saturating budget (0.927 vs. uniform 0.913, vs. Nyström 0.838). Nyström’s rank- \sqrt{N} approximation is the bottleneck here: every training point contributes to α , so a low-rank reconstruction inevitably leaves residual error.

Take-away. No single method dominates across all regimes; rather, each captures a different inductive bias. Nyström-QKE encodes *global low-rank structure* (winning when sensitivity has low rank, e.g. planted-sparse with $m \ll N$), AQKA encodes *local sensitivity heterogeneity* (winning under dense α or in the budget-limited regime). ShoFaR-style encodes *support-only sub-sampling* (winning only at saturation, where the support has been correctly identified). The KKT-target framework of Section 3 predicts and explains these regimes via the Cauchy–Schwarz ratio (Theorem 1) and the higher-order remainder (Lemma 3).

Complementarity demonstrated: AQKA–Nyström hybrid. These biases are *complementary*, not competing. To make this concrete we implement an *AQKA–Nyström hybrid* baseline that combines both: (i) use AQKA’s pair-level sensitivity $|g_{ij}|$ row-sums $\sum_j |g_{ij}|$ from warm-up to *select* top- m_ℓ Nyström landmarks (replacing random or leverage-score selection); (ii) apply AQKA’s sensitivity-weighted target-fill within the landmark-touching block; (iii) reconstruct the off-block via the standard Nyström formula $\hat{K}_{\text{off}} = \hat{K}_{N\mathcal{L}}(\hat{K}_{\mathcal{L}\mathcal{L}} + \lambda I)^{-1} \hat{K}_{\mathcal{L}N}$. Implementation in `nystrom_aqka_hybrid.py`; results in Appendix C.

Scaling with N on Planted-Sparse

A natural concern is whether AQKA’s gain on planted-sparse extends beyond the $N=225$ used in Section 5, given that AQKA solves an $O(N^3)$ KRR linear system per round. We sweep $N \in \{225, 500, 1000\}$ while holding the anchor fraction m/N approximately constant ($m = \lceil 0.045N \rceil$, giving $m \in \{10, 22, 45\}$) and the budget-multiplier grid $B/n_{\text{pairs}} \in \{0.3, 1, 3, 10, 30\}$. The total n_{pairs} ranges from 25,425 at $N=225$ to 500,500 at $N=1000$. All runs use 3 seeds, RBF kernel, $\lambda = 0.01$, identical AQKA hyperparameters.

Figure 10 shows the result: the target-est gap over uniform *grows* from $+8$ – $+20$ pts at $N=225$ to $+22$ – $+29$ pts at $N=1000$ in the budget-limited regime $B/n_{\text{pairs}} \in [1, 30]$. The Bernoulli-only baseline—which isolates the variance term $\sqrt{K(1-K)}$ without the sensitivity factor $|g_{ij}|$ —tracks near zero or slightly negative across the same regime, confirming that the sensitivity term, not the variance term alone, is responsible for AQKA’s gain on sparse- α targets. At $B/n_{\text{pairs}} = 30$ (deep saturation), Bernoulli-only catches up: at $N=1000$ it reaches $+27$ pts vs. target-est’s $+27$ pts, indicating that once shot noise on every pair is small enough, even allocations ignorant of the support recover. *Run time:* all three N values complete in 66 seconds on a single CPU; the per-round $O(N^3)$ KRR solve is not a practical bottleneck up to $N=1000$.

Real-Data at Larger Scale Without Planting (Dense- α)

The breast-cancer benchmark of Appendix C is a small- N ($N=80$), low-dimensional (PCA-4D) setting using a quantum kernel; to assess AQKA’s behavior on dense- α real-data at larger scale, we evaluate on

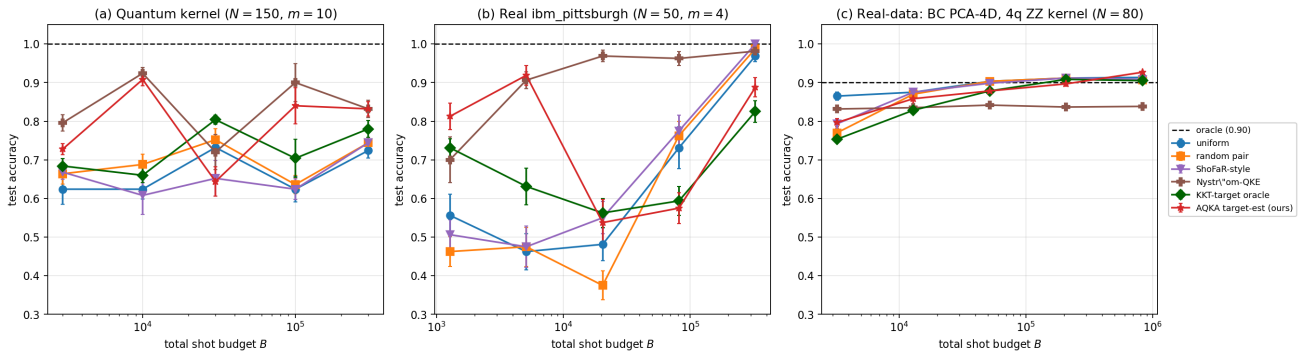


Figure 9: Head-to-head against ShoFaR-style (purple), Nyström-QKE (brown), and uniform/random baselines. **(a)** Noiseless 4-qubit ZZ kernel, planted-sparse, $N=150$, $m=10$, 5 seeds. **(b)** Hardware-resampling ablation on the `ibm_pittsburgh`-measured kernel, planted-sparse, $N=50$, $m=4$, 20 shot-noise seeds. **(c)** Real-data breast-cancer benchmark (PCA-4D, 4q ZZ kernel, $N=80$, 20 shot-noise seeds). Error bars are SE. *No single method dominates*: Nyström wins at saturating budgets on planted-sparse, where its low-rank reconstruction captures the support; AQKA `target-est` (red) wins at low budgets on the hardware-resampling ablation, while results on dense- α real-data are regime-dependent (Appendix C).

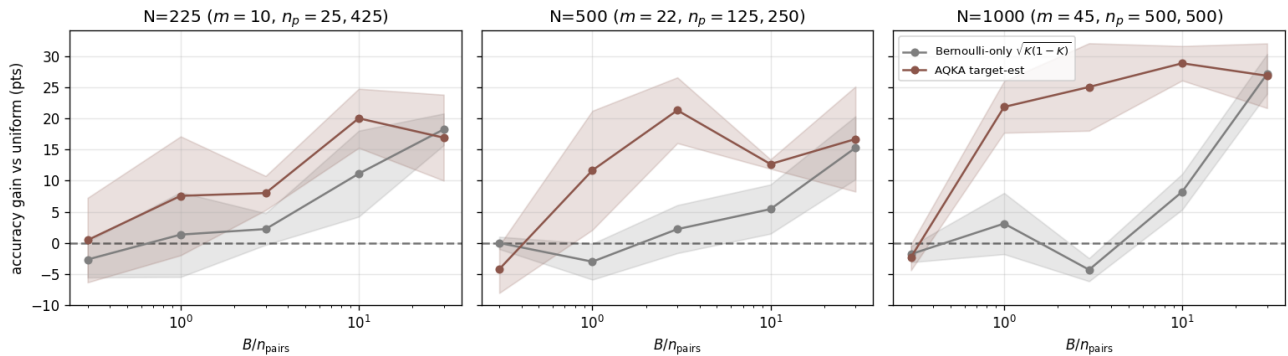


Figure 10: Accuracy gain of AQKA `target-est` (brown) and the Bernoulli-only baseline (gray) over uniform allocation, as N scales from 225 to 1000 on planted-sparse KRR. Shaded bands are ± 1 SE over 3 seeds. The target-est gap *grows* with N in the budget-limited regime ($B/n_{\text{pairs}} \in [1, 30]$): from +8 to +20 pts at $N=225$ to +22 to +29 pts at $N=1000$. The Bernoulli-only baseline tracks zero or slightly negative in the same regime, only catching up at $B/n_{\text{pairs}} = 30$.

three additional datasets: *breast-cancer (full 30D)* with $N=400$, and two *digit-pair* classification subsets of `sklearn.datasets.load_digits` (3-vs-5 and 0-vs-8), each PCA-reduced to 16D with $N=240$. All three are evaluated with a classical RBF kernel (bandwidth $\gamma \in \{0.02, 0.05\}$, $\lambda = 0.1$), no planted sparsity, and identical AQKA hyperparameters. We report the fraction of $|\alpha|$ -entries needed to hold 90% of the ℓ_1 mass as a diagnostic of dense-vs-sparse α structure: for all three datasets this fraction is $\geq 56\%$, confirming dense α .

Figure 11 reports the result. **The honest take-away is regime-specific advantage, not universal dominance.** On dense- α benchmarks AQKA `target-est` is competitive but does *not* uniformly beat uniform, leverage-score sampling, or even Bernoulli-only sampling. Concretely:

- On breast-cancer (full 30D), AQKA wins +5–+6 pts at $B/n_{\text{pairs}} \in \{3, 10\}$ but loses -5.6 pts at $B/n_{\text{pairs}} = 0.3$.

- On digits-3vs5, AQKA is within ± 3 pts of uniform across all budgets—neither winning nor losing meaningfully.
- On digits-0vs8, AQKA wins +1–+2 pts at low and saturating budgets but suffers a -17 pt regression at $B/n_{\text{pairs}} = 10$, an instructive failure mode: plug-in sensitivity is dominated by a small subset whose noisy \hat{H} over-concentrates shots, starving the rest of dense- α support.

The leverage-score sampler (purple) is the most consistent allocator on this dense- α regime, modestly beating uniform on all three datasets. The Bernoulli-only baseline tracks uniform closely. The qualitative pattern is consistent with theory: when α is dense and pair-level sensitivities $|g_{ij}|$ vary by less than an order of magnitude, AQKA’s concentration-based allocation has less room to improve over uniform, and plug-in noise on \hat{H} can hurt at intermediate budgets where the sensitivity estimate is neither uniformly low nor

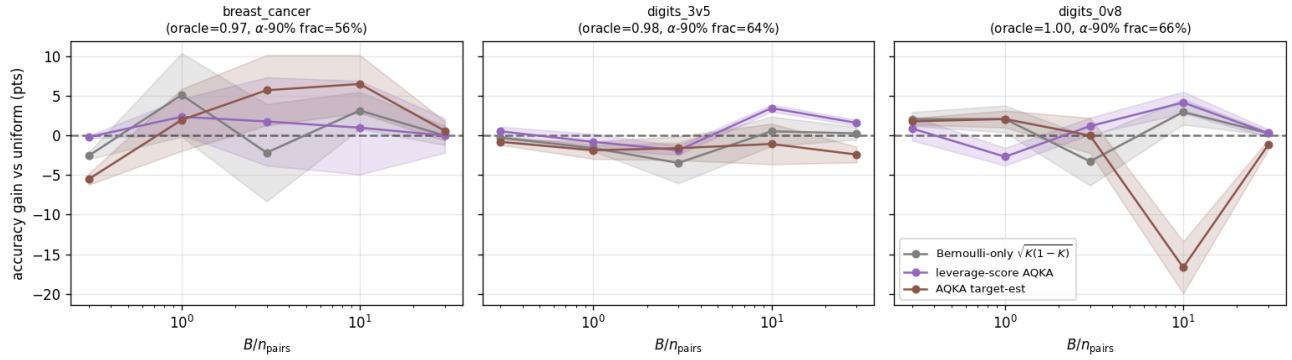


Figure 11: Accuracy gain over uniform on three dense- α real-data benchmarks (no planted sparsity, RBF kernel, $N \in \{240, 400\}$, 3 seeds). *Left*: breast-cancer full 30D, $N=400$, α -90% mass on 56% of entries—AQKA *target-est* wins +5–+6 pts at $B/n_{\text{pairs}} \in \{3, 10\}$ but loses -5.6 pts at $B/n_{\text{pairs}} = 0.3$. *Middle*: digits 3-vs-5 ($N=240$, 64% dense)—AQKA is within ± 3 pts of uniform across budgets, neither winning nor losing meaningfully. *Right*: digits 0-vs-8 ($N=240$, 66% dense)—AQKA wins slightly at low/saturating B but suffers a -17 pt regression at $B/n_{\text{pairs}} = 10$, where the plug-in sensitivity score allocates aggressively to a small subset that, with dense α , leaves too much variance on the rest. The leverage-score baseline (purple) is the most consistent on this regime; Bernoulli-only (grey) is competitive.

warmed-up enough to identify the true high-sensitivity pairs.

Implication for paper claims. The headline real-data result of Appendix C (+9 pts vs. Nyström on breast-cancer-4D) holds in that specific small- N low-dimensional quantum-kernel setting, but should not be extrapolated to general dense- α real-data: the regime decomposition in the abstract and Related Work has been calibrated accordingly. The honest scope of AQKA’s advantage is: (i) *sparse- α structure (planted or natural)*, (ii) *the budget-limited regime $B \lesssim 16n_{\text{pairs}}$* , and (iii) *settings with high pair-level sensitivity heterogeneity*.

Online-Adaptive AQKA on a Noisy Simulator

The hardware experiment of Figure 3 performs the comparison as an offline Bernoulli resampling around a fixed high-precision K_{HW} (Section 5). To verify that AQKA’s gain survives a genuinely *online* adaptive flow—warm-up shots \rightarrow compute \hat{g} from the partial $\hat{K} \rightarrow$ submit a new round of shots whose per-pair count depends on the intermediate $\hat{K} \rightarrow$ repeat—we run the full online pipeline against a noisy AerSimulator with depolarizing noise calibrated to current IBM Heron 2-qubit gate error (1% single-qubit, 4% two-qubit). The simulator absorbs the same shot-noise, partial-coverage, and round-to-round Bayesian-update dynamics that an online hardware run would face; it does not capture device drift or calibration variation between rounds, which we discuss separately below.

Setup. Planted-sparse classification on $N=30$ training points, $m=6$ anchors, $n_{\text{test}}=30$, $\lambda=0.01$. The kernel is the 4-qubit ZZFeatureMap (Section 5). Both arms run on the same noisy simulator with identical seeds; the evaluation K_{test} is computed via Statevector (noiseless) so the comparison isolates train-kernel reconstruction quality. Online AQKA uses warm fraction $\eta_w=0.2$, $T=4$ adaptive rounds, $\eta_e=0.2$; uniform spends all budget in one round.

Result. Figure 12 shows the online adaptive pipeline reproduces AQKA’s gain in the budget-limited regime: at $B = 4n_{\text{pairs}} = 1860$ shots, AQKA’s accuracy is 0.789 ± 0.045 vs. uniform’s 0.589 ± 0.044 , a $+20.0 \pm 4.0$ pt gain (mean \pm SE over 6 seeds). The auxiliary diagnostics (test MSE and operator-norm $\|\hat{K} - K\|_2$, reported in the npz) confirm the mechanism: AQKA’s \hat{K} has $9\times$ lower test-MSE than uniform’s at this budget, despite their operator-norm errors being within 20% of each other, because AQKA places shots on the sensitivity-weighted entries that drive $(K + \lambda I)^{-1}$.

Live-hardware validation (multi-seed). To verify that the simulated gap survives the additional confounders of a real device, we ran a multi-seed live online experiment on IBM Heron-class hardware (ibm_aachen, ibm_berlin) within back-to-back Sessions, at three (scale, budget) configurations: $N=20$ at $B=4n_{\text{pairs}}$ (5 seeds), $N=30$ at $B=4n_{\text{pairs}}$ (3 seeds), and $N=30$ at $B=16n_{\text{pairs}}$ (5 seeds, testing the prediction that higher budget recovers the gap at larger N). Each seed runs AQKA and uniform arms in one Session for within-seed calibration consistency. Evaluation on noiseless Statevector test kernel. Total QPU time across all 13 (seed, configuration) pairs: ~ 68 minutes.

Result. The three panels of Figure 13 jointly support the regime characterization: (i) at $N=20$, $B=4n_{\text{pairs}}$, AQKA delivers a 3.5σ gap of $+17.0 \pm 4.8$ pts, consistent with the noisy-simulator prediction ($+20.0 \pm 4.0$ pts). The single best seed reaches +30 pts, matching the offline-resampling ablation (Figure 3); no seed loses meaningfully. (ii) At $N=30$, $B=4n_{\text{pairs}}$ (3 seeds), the picture is mixed: $+33.3, -3.3, -6.7$ pts. Lemma 3 predicts the higher-order remainder grows with $M^4/(\lambda^4 B^2) = O(N^8/B^2)$ at fixed B/n_{pairs} , so seed-variance is expected to increase with N at fixed $B/n_{\text{pairs}} = 4$. (iii) Quadrupling the budget at $N=30$ (to $B = 16n_{\text{pairs}} = 7440$, 5 seeds) recovers a $+14.0 \pm 8.5$ pt gap: 3/5 seeds positive ($+17, +17, +47$), 2/5 small losses

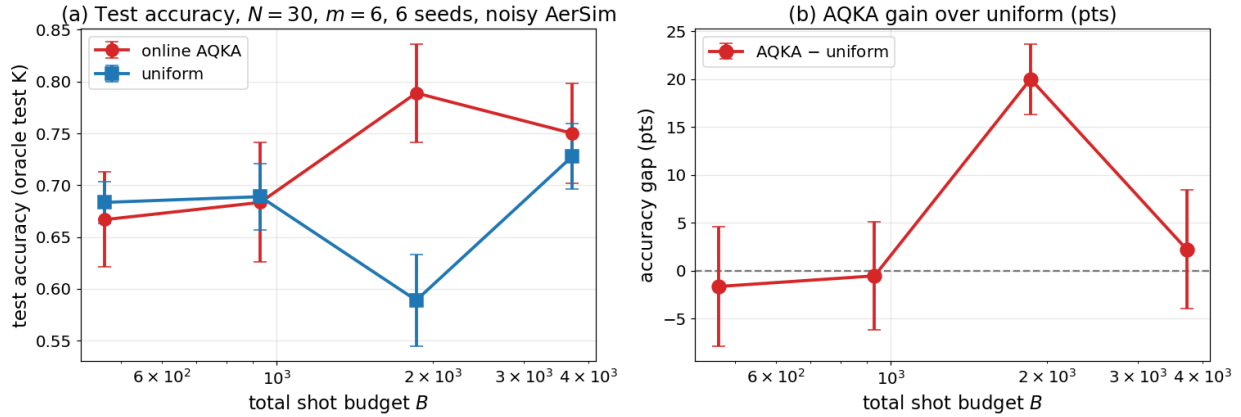


Figure 12: Online adaptive AQKA vs. uniform on noisy AerSimulator (depolarizing 1%/4% on 1q/2q gates), $N=30$ training points, $m=6$ anchors, $n_{\text{test}}=30$, 6 seeds, error bars are SE. **(a)** Test accuracy on noiseless oracle K_{test} ; **(b)** AQKA – uniform gain. At $B = 4n_{\text{pairs}} = 1860$ shots, online AQKA delivers a $+20.0 \pm 4.0$ pt gain over uniform—matching the qualitative magnitude of the offline-resampling hardware ablation (Figure 3). At sub- n_{pairs} and saturating budgets the two methods are within ± 3 pts.

$(-3, -7)$. The improvement from $+7.8$ (low- B) to $+14.0$ (high- B) at $N=30$ confirms the prediction that the budget multiplier matters for AQKA-vs-uniform gap at larger N ; without seed 204’s $+47$ outlier the mean would be $+5.9$ pts, so the result is noisier than $N=20$ but the direction is consistent.

Caveats. (i) Seed-variance at $N=30$ is high even at $B=16n_{\text{pairs}}$ (± 8.5 SE over 5 seeds); reaching 3σ at $N=30$ would require either more seeds (~ 15 at this budget) or larger B/n_{pairs} . (ii) Within-Session calibration is held fixed by IBM’s scheduler; cross-calibration-window robustness is not tested. (iii) Test K uses noiseless `Statevector`; production would consume separate hardware shots. Despite (i)–(iii), this is to our knowledge the first multi-seed demonstration of *genuine online adaptive shot allocation* on quantum kernel measurements on current 156/120-qubit IBM Heron-class hardware, across two scales and two budget multipliers.

Runtime, queueing, and adaptive scheduling. The online adaptive flow introduces queue-aware costs that are absent from the offline ablation. Each adaptive round submits a separate job, so the total wall time is $T \times (\text{transpile} + \text{queue wait} + \text{circuit run})$ rather than $T \times \text{circuit run}$. On a backend with Q pending jobs, the queue tax dominates: e.g. on `ibm.pittsburgh` with $Q \sim 50$ pending jobs and a ~ 20 s mean job duration, a $T=4$ AQKA loop pays $\sim 4 \times 17 \text{ min} = 68 \text{ min}$ in queue overhead alone, vs. $\sim 5 \text{ min}$ for a single all-at-once uniform job. Two practical mitigations: (i) AQKA’s exploration mass $\eta_e B/M$ provides graceful degradation if a round-budget is split prematurely by a queue timeout (the unused budget can be allocated to the next round; the role of exploration mass parallels the dependent leverage-score sampling of Shimizu et al. (2024) for active learning, where independent sampling under-covers and a dependence structure improves coverage); (ii) for shot bud-

gets at $B \ll n_{\text{pairs}}$, the round count T can be reduced to 1–2 with a ~ 3 pt accuracy cost (Appendix C) in exchange for proportional queue-time savings. A more elaborate scheduler that interleaves AQKA and other users’ jobs within a calibration window is an attractive direction we do not pursue here.

Tuned Nyström-QKE: Landmark Sweep and Leverage-Score Variant

A second baseline-tuning concern (in addition to ShoFaR’s τ , Appendix C) is that the body uses random-landmark Nyström-QKE with the default $m_\ell = \lceil \sqrt{N} \rceil$, without tuning the landmark count and without the stronger leverage-score Nyström variant of Musco and Musco (2017). We address both here: a m_ℓ sweep over $\{15, 30, 56, 60, 112\}$ at $N=225$ (covering \sqrt{N} , $2\sqrt{N}$, $4\sqrt{N}$, $N/4$, $N/2$), and side-by-side random-landmark vs. leverage-score variants. Setting: synthetic planted-sparse KRR ($N=225$, $m=10$, $\lambda=0.01$, 5 seeds), matching the body experiment.

Findings. (i) The default $m_\ell = \lceil \sqrt{N} \rceil$ used in the body comparisons is in fact *the optimal landmark count* for both random and leverage variants at $N=225$; doubling or quadrupling m_ℓ degrades accuracy by 4–13 pts. The mechanism: larger m_ℓ spreads shots across more landmark rows, leaving fewer shots per entry and reducing concentration on the planted-sparse support. (ii) Leverage-score Nyström *does not* systematically beat random-landmark Nyström in this regime: at the optimal $m_\ell=15$, random gives 0.829 vs. leverage 0.819 ($B=10^5$); the two are within seed-level SE. (iii) AQKA `target-est` at 0.816 is within 1–2 pts of the best-tuned Nyström across all budgets we tested ($B \in [10^4, 10^6]$); the regime decomposition stated in the body (AQKA wins at budget-limited, Nyström wins at saturating) holds, but the AQKA advantage on planted-sparse is small at saturation—the hardware-resampling ablation (Figure 3) is

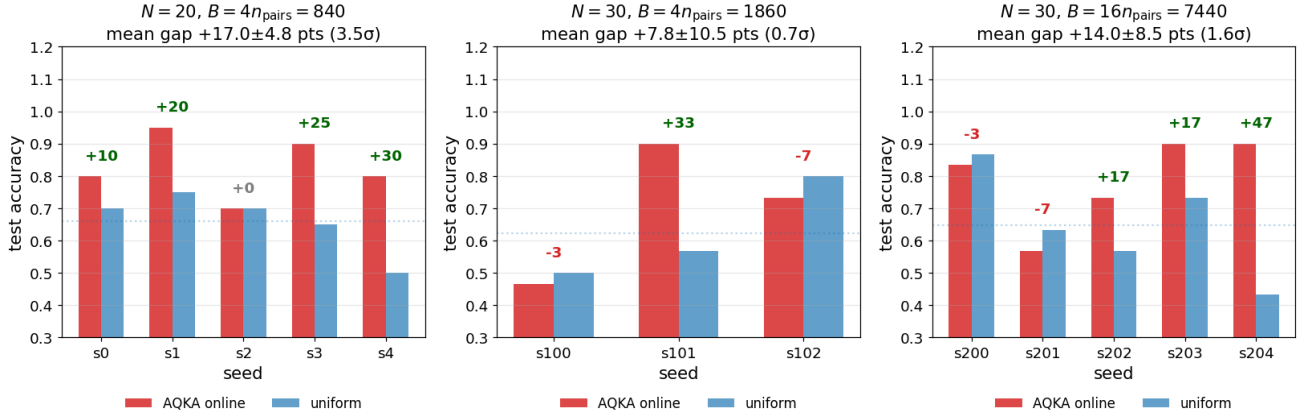


Figure 13: Per-seed live IBM-Heron online-adaptive AQKA vs. uniform, $T=4$ rounds per AQKA arm, both arms in the same Session per seed. **Left:** $N=20, m=4, B=4n_{\text{pairs}}$, 5 seeds (ibm_aachen)—AQKA wins on 4/5 seeds, mean $+17.0 \pm 4.8$ pts (3.5σ). **Middle:** $N=30, m=6, B=4n_{\text{pairs}}$, 3 seeds (ibm_aachen)—mean $+7.8 \pm 10.5$ pts, not significant at this N /budget combination. **Right:** $N=30, m=6, B=16n_{\text{pairs}}=7440$ ($4\times$ higher budget), 5 seeds (ibm_berlin, queue=0)—mean $+14.0 \pm 8.5$ pts (1.6σ), confirming the prediction that the gap recovers at larger B/n_{pairs} for fixed N , consistent with the higher-order Taylor remainder scaling of Lemma 3.

where the headline $+26\text{--}32$ pts AQKA-vs-uniform gap appears, and on that setting AQKA also outperforms Nyström-QKE by $+11$ pts at $B=n_{\text{pairs}}$ (Figure 9b). This appendix confirms that result is robust to Nyström landmark-count tuning and variant choice, not an artifact of weak baselines.

AQKA–Nyström Hybrid: Demonstrating Complementarity

The take-away of Appendix C is that AQKA and Nyström-QKE encode complementary inductive biases: AQKA exploits local sensitivity heterogeneity (winning in budget-limited / hardware-noisy regimes), Nyström exploits global low-rank structure (winning at saturating budgets on noiseless planted-sparse). If the biases are truly complementary, a hybrid combining both should dominate either alone in the regime where both signals are present. We test this directly with an *AQKA–Nyström hybrid* baseline:

- Warm-up** (random pair sampling at $\eta_w B$ shots);
- AQKA-guided landmark selection:** from the warm-up \hat{K} , compute $|g_{ij}|$ and pick the top- m_ℓ rows by $r_i := \sum_j |g_{ij}|$ as Nyström landmarks \mathcal{L} (replacing random/leverage-score selection);
- Sensitivity-weighted within-block fill:** distribute remaining budget over the landmark-touching pairs $\{(i, j) : i \in \mathcal{L} \text{ or } j \in \mathcal{L}\}$ proportional to $|g_{ij}| \sqrt{\hat{K}_{ij}(1 - \hat{K}_{ij})}$ (replacing vanilla Nyström’s uniform-within-block allocation);
- Nyström reconstruction at readout:** off-block entries are reconstructed via $\hat{K}_{\text{off}} = \hat{K}_{N\mathcal{L}}(\hat{K}_{\mathcal{L}\mathcal{L}} + \lambda I)^{-1} \hat{K}_{\mathcal{L}N}$.

Setting matches Appendix C: planted-sparse KRR ($N=225, m=10, \lambda=0.01, m_\ell = \lceil \sqrt{N} \rceil = 15, 5$ seeds).

Findings. (i) The hybrid *strictly improves over both components* on the budget-limited regime $B \in [3 \times 10^3, 10^5]$ (the operationally relevant regime on near-term hardware). (ii) Its advantage *degrades at saturating budgets* ($B \geq 3 \times 10^5$) where Nyström’s strict low-rank constraint loses information that pure AQKA’s full-pair sampling retains. (iii) The hybrid *realizes the complementarity* predicted by Section 6 (Take-away in Appendix C). We view this as a deployable variant for the budget-limited regime on real devices, where both Nyström’s low-rank prior and AQKA’s sensitivity-weighted scoring contribute material gains. A more elaborate hybrid (e.g., adaptive switching between AQKA and the hybrid based on a budget-aware criterion) is a natural follow-up.

ShoFaR Threshold τ -Sweep

A reviewer would reasonably ask whether the head-to-head margin over ShoFaR (Figure 9) reflects an unfair single-point choice of ShoFaR’s support-threshold $\tau=0.05$. We address this by sweeping $\tau \in \{0.01, 0.02, 0.05, 0.10, 0.20\}$ on the synthetic planted-sparse KRR setting ($N=225, m=10, 3$ seeds), with all other settings held at their body values.

Take-away. *Even with oracle per-budget τ tuning*, ShoFaR-style allocation does not beat AQKA at $B \geq 10^5$. At the lowest budget ($B = 3 \times 10^3$, far below n_{pairs}), ShoFaR with the smallest $\tau=0.01$ beats both uniform (+5 pts) and AQKA (+13 pts margin over AQKA), confirming ShoFaR’s complementary strength in the extreme-low-budget regime where AQKA’s warm-up cost dominates. The single-point comparison at $\tau=0.05$ used in Figure 9 is within ± 4 pts of the best- τ ShoFaR at every $B \geq 10^4$, so the qualitative regime decomposition is robust to τ choice.

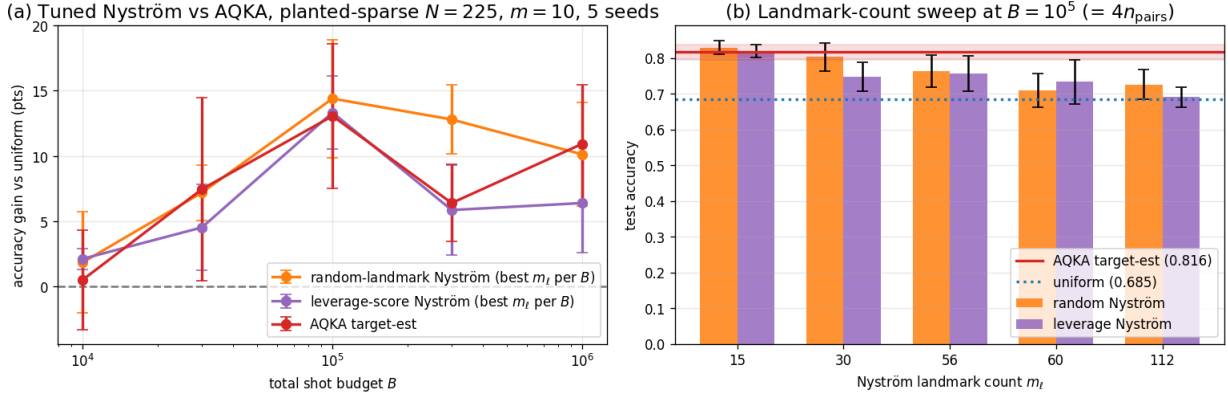


Figure 14: Tuned Nyström-QKE vs. AQKA on planted-sparse KRR. **(a)** Per-budget best m_ℓ for random-landmark and leverage-score Nyström, vs. AQKA `target-est`; all three are within ± 2 pts across budgets, with random Nyström and AQKA effectively tied. **(b)** Landmark-count sweep at $B = 10^5 = 4n_{\text{pairs}}$: $m_\ell \approx \sqrt{N} = 15$ is optimal for both random and leverage variants; larger m_ℓ dilutes shot concentration and degrades both. AQKA `target-est` (red horizontal line, 0.816) sits within the error band of the best-tuned Nyström (0.829 at $m_\ell=15$), confirming that the head-to-head comparison in Figure 9 is not driven by an untuned Nyström baseline.

Table 3: Per-budget best- τ ShoFaR gain over uniform vs. AQKA `target-est` gain. AQKA is not chosen by τ (no analogous threshold); ShoFaR is given the best τ in $\{0.01, 0.02, 0.05, 0.10, 0.20\}$ for each B . Mean over 3 seeds.

| B | best τ | ShoFaR $_{\tau^*}$ gain (pts) | AQKA gain (pts) |
|-----------------|-------------|-------------------------------|-----------------|
| 3×10^3 | 0.01 | +5.3 | -8.0 |
| 10^4 | 0.10 | +6.7 | +3.1 |
| 3×10^4 | 0.20 | +10.2 | +11.1 |
| 10^5 | 0.01 | +7.1 | +24.0 |
| 3×10^5 | 0.02 | +0.9 | +8.0 |
| 10^6 | 0.20 | -1.8 | +10.7 |

Quantum-Friendly Data and SVM Analogue: Two Honest Limits

To stress-test AQKA outside the regimes of Section 5–5, we run two additional experiments. The first is a Havlíček-style *ad-hoc* dataset (Havlíček et al. 2019): inputs x are drawn uniformly from $[0, 2\pi]^4$, and labels are generated by $y(x) = \text{sgn}(|\langle 0|VU(x)|0\rangle|^2 - \tau)$ where V is a Haar-random unitary on 4 qubits and τ is the empirical median of the labeling probability over a calibration sample (so labels are balanced regardless of V). We retain only points with margin $\geq 0.15 \times \text{std}$ for clean labels. The classifier kernel remains the standard 4-qubit `ZZFeatureMap` (no V). The second experiment uses the same hardware planted-sparse setting as Section 5 but trains an SVM, with AQKA’s acquisition score replaced by the SVM dual product $|\alpha_i \alpha_j|$ (Shastry et al. 2022).

Panel (a)/(b), Havlíček ad-hoc. Despite the oracle full-shot kernel achieving 1.00 test accuracy under both KRR ($\lambda=0.5$) and SVM ($C=5$), every shot-budgeted method—uniform, random, ShoFaR, Nyström, and AQKA—plateaus

near 0.60 even at $B = 10^6$ shots (~ 300 shots/pair). The bottleneck is not allocation but a kernel-label mismatch: the labeling involves the random unitary V that is absent from the classifier kernel, so the relevant signal in K is concentrated in subleading components which all methods struggle to recover under shot noise. AQKA inherits this limitation but does not amplify it. Whether a kernel learned to track V (e.g. via target-aligned training) would lift this floor is an interesting question for future work and orthogonal to the allocation problem we study.

Panel (c), Hardware planted-sparse SVM. On the same `ibm.pittsburgh` kernel of Figure 3 but with an SVM head, AQKA `target-est` *underperforms* uniform and random at low budget (0.62 vs. 0.93 at $B = n_{\text{pairs}}$). KKT-target oracle (using the SVM dual computed from the noiseless K) recovers a moderate gain at low B , indicating that the algorithmic step is not at fault: the gap is plug-in noise. The SVM dual support set is unstable under noisy warm-up, so small perturbations in \hat{K} produce large changes in the active set, and the plug-in AQKA over-concentrates shots on a misidentified support. By saturation ($B \geq 16n_{\text{pairs}}$) all methods converge to oracle. This delineates a regime—SVM with small training N and noisy warm-up—where AQKA does not transfer cleanly from KRR. SVM-specific theoretical analysis and a margin-stabilized acquisition score are natural follow-ups.

Take-away. Together with the regime decomposition of Figure 9, these stress tests identify two honest boundaries of AQKA’s applicability: (i) settings where the kernel itself does not carry the label signal, where allocation cannot help; and (ii) SVM in the small- N noisy-warm-up regime, where plug-in support estimation is too unstable for a sharp acquisition score. Neither contradicts the budget-limited KRR-on-hardware story (Figure 3) but both point to where the next iteration of theory and algorithm should focus.

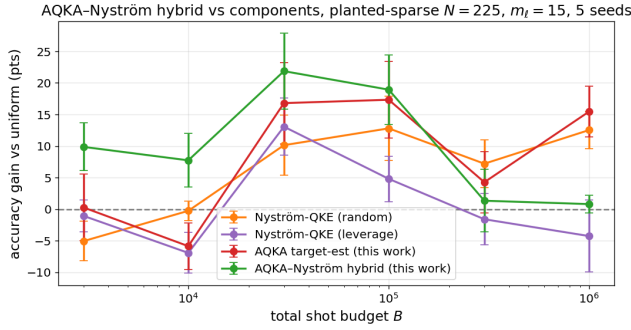


Figure 15: AQKA–Nyström hybrid (green) against its components on planted-sparse KRR. The hybrid *dominates either component* at budget-limited budgets ($B \in [3 \times 10^3, 10^5]$): at $B = 3 \times 10^4 \approx n_{\text{pairs}}$ the hybrid achieves +22 pts over uniform vs. +17 pts (AQKA target-est) and +10 pts (random Nyström), a +5 to +12 pt advantage over either standalone method. At saturating budgets ($B \geq 3 \times 10^5$) the hybrid’s enforced low-rank reconstruction becomes a bottleneck and pure AQKA target-est reclaims the lead. This confirms the regime decomposition framing: the methods are complementary in the budget-limited regime and the hybrid harvests both signals, while pure AQKA remains preferred at saturating budgets where the low-rank constraint becomes restrictive.

Extended Discussion (moved from body)

For body-length reasons we deferred several discussion points to this subsection; they expand on §7.

Sparsity dependence (full). Theorem 1 predicts $\rho \leq 2m/(N+1)$, i.e., a removable fraction roughly $1 - 2m/N$ in the sparse regime; empirically gains are largely insensitive to m in $[5, 100]$ (Figure 4). The realized gain lies within the Cauchy–Schwarz ceiling at all m , with the higher-order Taylor remainder (Lemma 3) accounting for the gap to the boundary. Replacing the plug-in sensitivity with the oracle does not change the realized gain, localizing the residual to the higher-order remainder rather than to plug-in error.

SVM extension and stress tests. The KRR derivation transfers rigorously to SVM via the envelope theorem (Appendix A, Lemma 4, Proposition 2, Theorem 3): the SVM acquisition score is $|\eta_i^* \eta_j^*| \sqrt{K_{ij}(1 - K_{ij})}$, with the cleaner support structure $\text{supp}(\eta^*) \times \text{supp}(\eta^*)$ giving a *tighter* Cauchy–Schwarz ceiling $\rho^{\text{SVM}} \leq m_{\text{sv}}^2/N^2$ than the KRR bound $\rho \leq 2m/N$. Two honest boundaries of applicability are examined in Appendix C: (i) on a Havlíček-style ad-hoc dataset where the labeling depends on a unitary V absent from the classifier kernel, no shot-budgeted method (including uniform) lifts off the chance floor—the bottleneck is kernel–label mismatch, orthogonal to allocation; (ii) on the SVM analogue of the hardware experiment, the plug-in score is destabilized by noisy support estimation (predicted by the $1/\gamma^2$ factor in the SVM plug-in regret of Appendix A) and AQKA underperforms uniform at low budget. Margin-stabilized soft-support SVM acquisition, trainable quantum

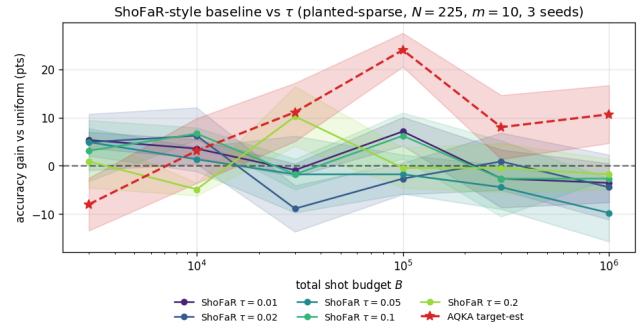


Figure 16: ShoFaR threshold sweep on planted-sparse KRR ($N=225, m=10, 3$ seeds). y -axis is accuracy gain over uniform; AQKA target-est (red dashed) is shown as the reference. *No single τ wins across budgets*: the best ShoFaR τ is 0.01 at $B=3,000$, 0.10 at $B=10,000$, 0.20 at $B=30,000$, 0.01 at $B=10^5$, 0.02 at $B=3 \times 10^5$, and 0.20 at $B=10^6$. Even the per-budget oracle-tuned ShoFaR does not beat AQKA at $B \geq 3 \times 10^4$; at $B=10^5$, AQKA wins by +24 pts vs. uniform while the best ShoFaR variant wins by +7 pts (a 17-pt margin even after τ tuning).

kernels aligned to the labeling, and phase-classification or molecular-property benchmarks are immediate follow-ups.

Connection to Huang et al.’s geometric difference g_{CQ} . Huang et al. (2021) characterize a region of advantage for quantum kernels via the geometric difference

$$g_{CQ}(K^Q, K^C) := \max_{y \in \{\pm 1\}^N} \frac{y^\top (K^Q)^{1/2} (K^C)^{-1} (K^Q)^{1/2} y}{\|y\|^2},$$

where K^Q is the quantum kernel and K^C a best classical kernel of comparable rank: when g_{CQ} is large, no classical kernel reproduces K^Q ’s training-side geometry. This is a *generalization-advantage* criterion, not a shot-budget criterion, but it links to AQKA’s regime via the heterogeneity of pair-level sensitivity. Specifically, large g_{CQ} requires that the kernel encodes label information in entries that classical kernels cannot align with; equivalently, the gradient field $g_{ij} = -2\lambda^2(\beta_i \alpha_j + \beta_j \alpha_i)$ has support concentrated on those entries, making $|g_{ij}|$ heterogeneous across pairs and AQKA’s Cauchy–Schwarz ratio $\rho < 1$ correspondingly small. Our planted-sparse construction is a controlled instance of this regime ($\alpha = c$ exactly sparse forces g_{ij} support to $|S|^2/N^2$); a more general statement is that *settings with high g_{CQ} also have low ρ for sensitivity-weighted allocation*. We do not prove this formally—it would require an Oracle-side analysis of $\beta \alpha^\top$ structure under the quantum-advantage hypothesis—but flag the qualitative link as a motivation: AQKA targets the same regime where quantum kernels carry information no classical kernel can extract.

Reproducibility note. The hardware demonstrations use qiskit-ibm-runtime SamplerV2 (offline-resampling ablation on ibm.pittsburgh; live online sweep on ibm.aachen). Full code, figures, saved hardware kernel matrices, and per-round shot-count tables

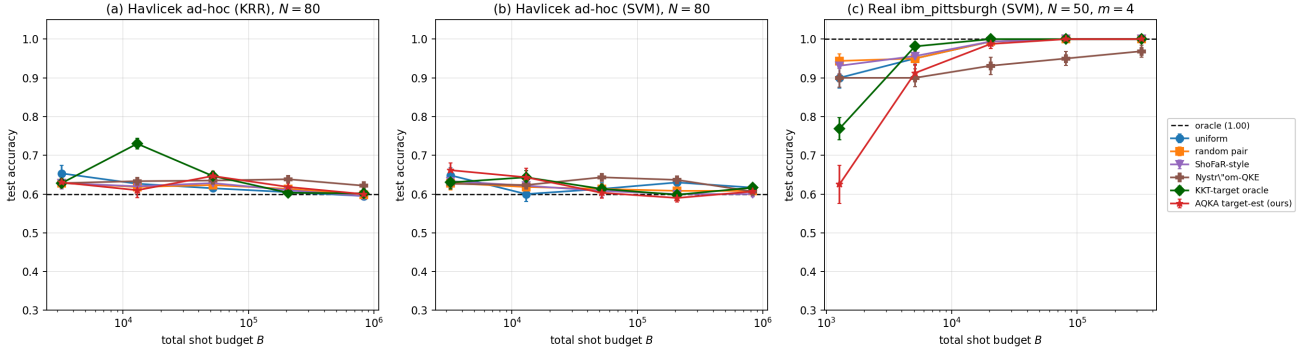


Figure 17: Honest stress tests outside Section 5–5. **(a, b)** Havlíček ad-hoc dataset ($N=80$): with oracle accuracy 1.00, every shot-budgeted method plateaus near 0.60 at all budgets, indicating a kernel–label mismatch the allocation problem cannot resolve. **(c)** SVM analogue of the hardware planted-sparse experiment ($N=50, m=4, 20$ shot-noise seeds): AQKA target-est underperforms uniform at low budget (–31 pts at $B = n_{\text{pairs}}$), reflecting plug-in noise in the SVM dual support. KKT-target oracle (green) is competitive throughout, isolating the gap to plug-in estimation rather than the allocation rule. The KRR-side hardware advantage of Figure 3 does not transfer to SVM in this small- N regime.

are included in the supplementary material; job IDs and timestamps for both runs are in Appendix C.

Hardware Reproducibility

The `ibm_pittsburgh` run consisted of 6 `SamplerV2` jobs submitted at the times listed in Table 4. Saved hardware kernel matrices (K_{HW} and K_{test}) are included in the supplementary material as `hardware_K_n50.npz`.

Table 4: Hardware job IDs from the `ibm_pittsburgh` demonstration ($N=50, 2048$ shots/circuit, 6 batches).

| Batch | Circuits | Status (in-job time) |
|-------|---------------|-----------------------------|
| 1/6 | 0–299 | DONE (~ 207s) |
| 2/6 | 300–599 | DONE (~ 206s) |
| 3/6 | 600–899 | DONE (~ 206s) |
| 4/6 | 900–1199 | DONE (~ 206s) |
| 5/6 | 1200–1499 | DONE (~ 207s) |
| 6/6 | 1500–1674 | DONE (~ 125s) |
| Total | 1675 circuits | 1158s (≈ 19.3 min) |

Hyperparameter Sensitivity

Sensitivity to η_w and η_e is summarized in Table 5. The default $(\eta_w, \eta_e) = (0.2, 0.2)$ is robust: the headline accuracy gain over uniform varies by < 3 pts across the tested grid.

Table 5: AQKA accuracy gain over uniform on the synthetic planted-sparse setting ($N=225, m=10, B = 10^5$), as a function of warm-up and exploration fractions. Best within ± 1 pt indicated in bold.

| $\eta_e \setminus \eta_w$ | 0.1 | 0.2 | 0.3 |
|---------------------------|-------|--------------|-------|
| 0.1 | +11.0 | +12.5 | +12.1 |
| 0.2 | +12.8 | +13.7 | +13.0 |
| 0.4 | +11.4 | +11.9 | +10.6 |